Volume 1103 22 March 2020 ISSN 0003-2670

ELSEVIER

Analytica Chimica Acta

AN INTERNATIONAL JOURNAL DEVOTED TO ALL BRANCHES OF ANALYTICAL CHEMISTRY

On the competition between mixing rate and uniformity in a coaxial hydrodynamic focusing mixer

Diego A. Huyke, Ashwin Ramachandran, Diego I. Oyarzun, Thomas Kroll, Daniel P. DePonte, Juan G. Santiago

(Published in pages 1–10 of this issue)

Analytica Chimica Acta 1103 (2020) 1–10

Contents lists available at ScienceDirect

Analytica Chimica Acta

journal homepage: www.elsevier.com/locate/aca

On the competition between mixing rate and uniformity in a coaxial hydrodynamic focusing mixer

Diego A. Huyke [a], Ashwin Ramachandran [b], Diego I. Oyarzun [a], Thomas Kroll [c], Daniel P. DePonte [c], Juan G. Santiago [a, *]

[a] Department of Mechanical Engineering, Stanford University, Stanford, CA, 94305, USA
[b] Department of Aeronautics & Astronautics, Stanford University, Stanford, CA, 94305, USA
[c] SLAC National Accelerator Laboratory, Menlo Park, CA, 94025, USA

HIGHLIGHTS

- Experimentally validated numerical and semi-analytical models for a coaxial mixer.
- Mixer is easy to fabricate and compatible with line-of-sight-integration detection.
- Mixer demonstrated order 100 μs mixing times and residence times of the same order.
- Studied details of tradeoff between mixing rate and the uniformity of mixing.
- Design can tune expansion of mixed stream to increase the detection signal.

GRAPHICAL ABSTRACT

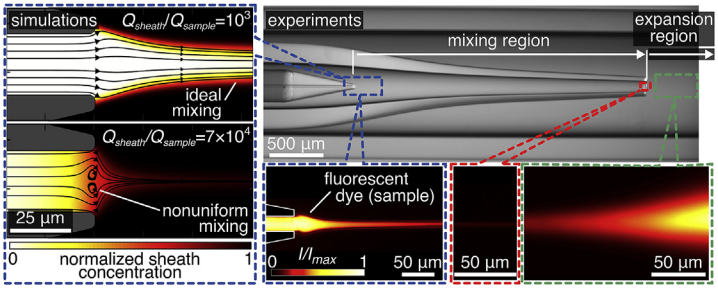

ARTICLE INFO

Article history:
Received 17 October 2019
Received in revised form
26 December 2019
Accepted 6 January 2020
Available online 8 January 2020

Keywords:
Microfluidics
Mixing
Hydrodynamic focusing
Coaxial capillaries
Kinetics

ABSTRACT

Fast microfluidic mixers for use with line-of-sight integrating detection schemes pose unique challenges. Such detectors typically cannot discriminate signal from slow moving (e.g. near internal walls) and fast-moving portions of the fluid stream. This convolves reaction rate dynamics with fluid flow residence time dynamics. Further, the small cross sections of typical three-dimensional hydrodynamic focusing devices lead to lower detection signals. The current study focuses on achieving both small time scales of mixing and homogenous residence times. This is achieved by injecting sample through a center capillary and hydrodynamically focusing using a sheath flow within a tapered second capillary. The current design also features a third, larger coaxial capillary. The mixed stream flows into the large cross-section of this third capillary to decelerate and expand the stream by up to 14-fold to improve line-of-sight signal strength of reaction products. Hydrodynamic focusing, mixing, and expansion are studied using analytical and numerical models and also studied experimentally using a fluorescein-iodide quenching reaction. The experimentally validated models are used to explore trade-offs between mixing rate and uniformity. For the first time, this work presents detailed analysis of the Lagrangian time history of species transport during mixing inside coaxial capillaries to measure mixing nonuniformity. The mixing region enables order 100 μs mixing times and residence time widths of the same order (140 μs).

* Corresponding author. 440 Escondido Mall, Bldg 530/224, Stanford, CA, 94305, USA.
E-mail address: juan.santiago@stanford.edu (J.G. Santiago).

https://doi.org/10.1016/j.aca.2020.01.013
0003-2670/

1. Introduction

Rapid microfluidic mixers have been critical in studies of protein folding [1–7], enzyme reactions [8–10], and cell activation [11,12], as well as leveraged in disease detection [13–15], drug development [16–18], and sequencing or synthesis of nucleic acids [19–21]. Lamination mixers are a class of passive microfluidic mixers wherein (internal flow) hydrodynamic focusing is used to mix a low flow rate reagent stream with a relatively high flow rate stream(s) containing at least one other reagent. These mixers typically use laminar, deterministic flows to create a large interface area between streams and to achieve small distances over which molecular diffusion must act to initiate chemical reactions. The goal of such lamination mixers is not to achieve uniform, global mixing of two streams but rather to mix the sheath species into the reactant within the sample stream to initiate a fast reaction confined to the sample stream. In this scenario, the sample species have a high molecular weight, such that their counter diffusion away from the sample stream is small. This approach enables minimizing flow rate (and consumption) of the sample stream reactant. As we shall discuss in this paper, this also enables a reaction to be initiated more uniformly among the various streamlines of the inlet sample streamline.

Lamination mixers can be divided into two main types: two-dimensional (2D) and three-dimensional (3D) mixers. 2D mixers employ channels fabricated within a single plane to effect 2D hydrodynamic flow patterns. These reduce a center reagent (sample) stream dimension in one direction normal to the main flow but not in the second dimension [5–7,22,23]. In contrast, 3D mixers confine a reagent stream in all directions normal to the flow so that sample streamlines are separated from walls during mixing. This is important as near-wall streamlines have much lower velocities and hence are associated with larger residence times within the mixer. Commonly, 3D mixers use axisymmetric mixing schemes in which a capillary injects a sample stream within an (annular) sheath stream [24–34]. A performance comparison of various 3D hydrodynamic focusing mixers is provided in Section S1 of the Supplementary Data.

2D mixers are typically suited for pointwise detectors (e.g. confocal microscopy [3–7,22,23]) which exclusively sample fast-moving and fast-mixing regions away from the mixer's internal walls. In turn, 3D mixers are well suited for detectors which line-of-sight integrate in a direction at angle with the flow (e.g. widefield microscopy [24,33,34] or X-ray detection [25,35]). The latter integration collects signal from both slow-moving (long residence time) regions near walls and fast-moving (short residence time) regions away from walls. For example, Pabit et al. [34] (and similarly Hamadani et al. [33]) used round capillaries within secondary, square capillaries and quenched a fluorescent stream (duration for 0.5× decrease in integrated intensity) in 600 μs. Burke et al. [24] improved on this architecture with a tapered inner capillary to decrease the time scale of momentum diffusion across the inner capillary annulus and reported a 50% drop in fluorescence intensity within 100 μs. Recently, Calvey et al. [28] and Plumridge et al. [25] developed mixers which achieve fast mixing by forcing flow into a downstream, small inner radius capillary for further acceleration. Plumridge et al. [25] demonstrated RNA folding using SAXS and reported dynamics at timescales of order 10 ms.

Significant challenges remain towards homogenous and fast 3D mixing applicable to order 1–100 ms reaction kinetics studies. For example, to our knowledge, homogenous mixing has not been quantitatively demonstrated in fast, coaxial capillary mixers. Moreover, trade-offs among time, degree, and homogeneity of mixing in such coaxial mixers have not been explored. Further, hydrodynamic focusing yields thin sample streams which may be expanded to improve post-mixing detection signal-to-noise ratio (SNR). Current expansion methods [5,7,25] are limited to device geometry and flow parameters which are typically dictated by mixing requirements.

We here present the modeling, design, fabrication, and quantitative experimental validation of an axisymmetric microfluidic mixer with homogenous, sub-millisecond mixing times and sample consumption of order 0.1–100 μL min^{-1}. The mixer decouples mixing dynamics and SNR requirements using a three-capillary system. As shown in Fig. 1, the sample stream flows out of a centered sample capillary with a tapered outer surface. The sample stream is hydrodynamically focused by fast-moving sheath flow provided by a middle capillary. The middle capillary's inner and outer walls are also tapered to further accelerate the flow and achieve a sub-micron sample stream radius. To improve detection SNR, the mixed sample and annular sheath streams are rapidly expanded as they flow into a larger outer (third) capillary. Importantly, the degree of this downstream expansion is decoupled from the flow parameters which govern mixing and is tunable by controlling flow conditions at both ends of the outer capillary. For example, we demonstrate a 14-fold expansion of the radius of a mixed stream. Numerical and semi-analytical models were developed to support design efforts and to quantify trade-offs among performance measures. These models were validated with experimental imaging and dye quenching.

2. Materials and methods

2.1. Experimental

2.1.1. Fabrication and flow control

As shown in Fig. 1, the mixer is an axisymmetric, three-capillary system [24,25,28,29,31,33,36]. The current design uses fused silica inner capillaries, and borosilicate glass middle and outer capillaries. However, we have built versions of our mixer wherein the outer (third) capillary is replaced with a polyimide tube, compatible with hard X-ray spectroscopy experiments (described in Section S10). The sample solution flows out of the innermost capillary ($R_{sa} = 13$ μm) and into the middle capillary (R_{sh} tapers from 200 to 50 μm), where it is hydrodynamically focused by a higher-velocity sheath solution before the mixed stream expands into an outermost capillary ($R_{pr} = 750$ μm). Fig. 1c shows the sharpened-pencil-like taper of the inner capillary nozzle, which was polished on a precision lapping wheel (Ultrapol End & Edge Polisher, Ultra Tec, USA). The middle capillary was tapered using a laser-based micropipette puller (P-2000, Sutter Instrument, USA). The inner, middle, and outermost capillaries are telescoped and interfaced with our fluid delivery systems using microfluidic tee junctions (PEEK tee, IDEX, USA). Mixers typically operated for 50–100 h prior to clogging. See Figs. S1, S2, and S3, respectively, details of device materials, fabrication, and flow control. We note that our current device requires manual assembly, but recent advances in the resolution of 3D printing technologies [37,38] may enable microfabrication of a monolithic chip.

Sample flow rates (Q_{sa}) in the range of 0.1–1 μL min^{-1} were provided with a custom pneumatic pressure system which consisted of a sealed glass bottle connected to a 17–170 kPa pressure regulator with 0.1% accuracy (McMaster-Carr, USA). In this range, Q_{sa} was measured within 10% accuracy using a liquid flow meter (SLG64-0075, Sensirion, Switzerland). High Q_{sa} (1–100 μL min^{-1}), sheath (Q_{sh}), and positive probe flow rates ($Q_{pr} > 0$) were provided, within 1% accuracy by a high-performance liquid chromatography (HPLC) pump (LC-20AD, Shimadzu Corp., Japan). $Q_{pr} < 0$ was achieved by using a splitter valve (Micro-splitter valve, IDEX Corp.,

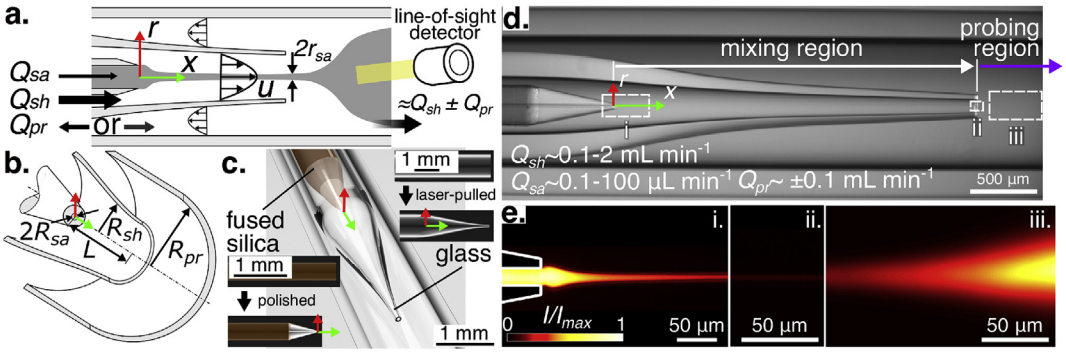

Fig. 1. (a) and (b) are schematics of the coaxial capillary device. The long taper of the middle capillary enhances hydrodynamic focusing while the large outer capillary enables radial expansion of the sample stream after mixing. Q_{pr} can be chosen to be negative (left arrow) or positive (right arrow). Here, R_{sa} = 13 µm, R_{sh} tapers from 200 to 50 µm, R_{pr} = 750 µm, and L = 3 mm. (c) Computer-aided design renders of device constructed from three telescoping fused silica and glass capillaries. (d) Experimental bright-field image of device. Indicated are typical flow rates. (e) Experimental epifluorescence images of a hydrodynamically focused dye stream (with Q_{sh} = 0.5 mL min^{-1} and Q_{sh}/Q_{sa} = 1000) as it exits the inner capillary aperture (i) and is further focused to r_{sa} = 1 µm (ii). Downstream, the sample stream radius expands (iii, here, Q_{sa}, Q_{sh}, and Q_{pr} were respectively 5, 500, and −60 µL min^{-1}).

USA) to increase the hydraulic resistance of the main outlet; see Section 3.4 for details.

2.1.2. Fluorescence quenching

To characterize mixer performance for all flow conditions, a 50 µM fluorescein sample was flowed into a pure buffer sheath (unquenched) and into a 500 mM KI sheath (quenched) [25,27,28]. All solutions were buffered with 20 mM Tris and 10 mM H−Cl (Sigma-Aldrich, USA) at a measured pH of 8. The rapid fluorescence quenching reaction enabled quantification of fluorescein and iodide transport. Fluorescein diffusivity [39] was taken as D_{sa} = 4.25 × 10^{-6}cm^2 s^{-1} and iodide diffusivity [5] was taken as D_{sh} = 2.5 × 10^{-5}cm^2 s^{-1}. As show in Fig. S4, the fluorescein-iodide quencher rate coefficient was obtained from preliminary experiments using a stopped-flow reaction chamber and found to be 7.29 M^{-1}.

2.1.3. Imaging and data processing

Epifluorescence experiments were performed on an inverted microscope (Eclipse TE 300E, Nikon, Japan) fitted with a filter cube (FITC-A-Basic, Semrock, USA) and a 20× magnification and 0.95 numerical aperture water immersion objective (MRD77200, Nikon, Japan). Illumination was provided using a high-power light-emitting diode (SOLIS-470C, Thorlabs, USA). Experimental images using a 0.5× demagnification lens and a scientific-grade complementary metal oxide semiconductor camera (sCMOS) (ORCA-Flash4.0 V2, Hamamatsu, Japan). Region-of-interest images were 100 µm wide and 1 mm long in object space. The image exposure time was varied between 1 and 4 ms to obtain image signal-to-noise ratios of order 100 to 1000.

Before data processing, all images were flat-field corrected [40] and spatially averaged along super-columns of 10 µm width (in x-direction of object plane). We estimate the width of the diffuse sample stream σ, by fitting a Gaussian distribution of the form $f(r) \sim e^{-r^2/\sigma}$ to image data within 80% of the maximum super-column intensity. To quantify quenching, pixel intensities were integrated as $\sum I_q(x,r)/\sum I(x,r)$ for superpixels regions equivalent to 4 µm in height (r-direction) and 10 µm in width (x-direction of object plane), as shown in Fig. S5. Here, I_q and I respectively denote the pixel intensities of the quenched and unquenched images. The area-averaged concentration of iodide inside of the sample stream is related to the integrated intensity ratio using a Stern-Volmer fit.

2.2. Numerical model

The mixer flow was analyzed using numerical solutions of the steady state, incompressible Navier-Stokes and convection-diffusion equations. The simulations were used to systematically explore mixer performance under varied flow conditions. A commercial nonlinear solver (COMSOL Multiphysics 5.4, COMSOL, Sweden) was used to solve for Eulerian-frame velocity and concentration fields. The model was applied to a mixer design that consisted of a three-capillary system, as shown in Fig. 1a. The model simulations were performed in two-dimensions (r and x) and assume axisymmetry. The state equations solved in the simulations are

$$\nabla \cdot \vec{u} = 0, \tag{1}$$

$$\rho(\vec{u} \cdot \nabla \vec{u}) + \nabla p - \eta \nabla^2 \vec{u} = 0, \text{and} \tag{2}$$

$$\nabla \cdot (-D_i \nabla c_i + c_i \vec{u}) = 0, \tag{3}$$

where $\vec{u}$ is the velocity with components u_x and u_r respectively in the x and r directions, ρ is the density, p is the pressure, η is the dynamic viscosity, and c_i and D_i are respectively the concentration and diffusivity of species i. Subscript i refers to either sample (sa) or sheath (sh) species. Equations (1)–(3) were subject to the boundary conditions

$$\vec{u}(\vec{x}_w) = 0 \text{ and} \tag{4}$$

$$\nabla c_i \cdot \hat{n} = 0, \tag{5}$$

where $\vec{x}_w$ denotes the location of walls and $\hat{n}$ is the unit normal vector at the wall. Equations (4) and (5) respectively represent no-slip and no penetration at the wall. Normal inflow velocity and fixed concentration boundary conditions where specified at the sample and sheath model inlets. Further, zero pressure and concentration outflow boundary conditions were specified at the model outlet.

2.3. Semi-analytical model

We also developed a computationally economic model for Eulerian-frame velocity and concentration fields in the device (cf.

Section S5). The model is "semi-analytical" in that it reduces to a rapidly solved numerical integration. As shown in Fig. 1a, this model assumes that the sheath flow rate Q_{sh} is much larger than sample flow rate Q_{sa}. We further assume that each section of the coaxial flow, within the tapered middle capillary, is locally Poiseuille (parabolic) flow with small radial velocity u_r (analogous to the lubrication theory approximation [41]). These assumptions lead to a near-centerline sample velocity U_{sa} which is locally uniform over the radius and equal to twice the sheath bulk velocity U_{sh} [41].

The rate of radial diffusion of sample and sheath species within small streamwise sections of the flow Δx is treated as radial diffusion within a cylinder at the local inner radius of the tapered middle capillary. Accordingly, for each short section Δx, transport of species i is governed by

$$\frac{\partial c_i^{(n)}}{\partial t} - D_i \frac{1}{r}\frac{\partial}{\partial r}\left(r\frac{\partial c_i^{(n)}}{\partial r}\right) = 0, \tag{6}$$

where n denotes a time step and, again, i denotes the species of interest.

Given boundary and initial conditions the analytical solution to equation (6) is used to obtain the evolution of concentration profiles over short time increments Δt equal to $\Delta x/U_{sa}$. The radial concentration profile for each time step n yields

$$c_i^{(n)}(r) = c_i^{(n)}(10r_{sa}^{(n)})\{1 - A^{(n)}\} + B^{(n)} \int_0^{10r_{sa}^{(n)}} J_0\left(ra_j^{(n)}\right) c_i^{(n-1)}\left(\frac{r_{sa}^{(n-1)}}{r_{sa}^{(n)}} r\right) r dr, \tag{7}$$

where

$$A^{(n)} = \sum_{k=1}^{\infty} \frac{J_0\left(ra_k^{(n)}\right) \cdot \exp\left(-D_i\left(a_k^{(n)}\right)^2 \Delta t\right)}{a_k^{(n)} \cdot J_1\left(10r_{sa}^{(n)} a_k^{(n)}\right) \cdot 5r_{sa}^{(n)}}, \tag{8}$$

$$B^{(n)} = \sum_{k=1}^{\infty} \frac{J_0\left(r\left(a_k^{(n)}\right)^2\right) \cdot \exp\left(-D_i\left(a_k^{(n)}\right)^2 \Delta t\right)}{J_1^2\left(10r_{sa}^{(n)}\left(a_k^{(n)}\right)^2\right) \cdot 50\left(r_{sa}^{(n)}\right)^2}, \tag{9}$$

r_{sa} is the non-diffuse sample stream radius (referring to Fig. 1a), and the a_{nk} are the roots of $J_0(10r_{sa}^{(n)} a_{nk}) = 0$, and J_0 is the Bessel function of the first kind of order zero [42]. The flow acceleration causes a stretching of sample fluid volumes which tends to decrease the radius of the diffusing sample stream. We account for this heuristically by re-scaling the r-coordinate of the concentration profile, consistent with conservation of mass. The latter assumes a high local Peclet number based on the radial inward velocity and the inner radius of the flow region. Equations (7)–(9) are computed for every n to find the sample and sheath concentration fields.

2.4. Mixing figures of merit

Our mixer is well suited for line-of-sight detectors that collect signal from all sample species within an inner-wall-to-inner-wall probe volume. Hence, to evaluate mixer performance, we chose the following depth-averaged figures of merit: mixing degree, mixing time, and mixing nonuniformity [5,6,23,40,43,44]. These are described quantitatively below.

We here define the mixing degree α in terms of a normalized, cross-section-area-averaged sheath concentration c_{sh} within the sample stream. We thus consider 100 sample streamlines uniformly seeded at $x = -2R_{sa}$, upstream of the inner capillary aperture, and define α as follows

$$\alpha(x) = \frac{\sum_j c_{sh}(x, r_j) 2\pi r_j \Delta r_j}{c_{sh,0}\pi r_{sa}^2}, \tag{10}$$

where j is the index of a streamline (with corresponding radial coordinate r_j), Δr_j is the radial distance between streamlines j and $j+1$, and $c_{sh,0}$ is the upstream sheath concentration. Note r_{sa} is a function of the flow conditions and α starts at zero and tends to unity as the sheath mixes into the (centered) sample stream tube.

The mixer is designed to study reaction kinetics. Hence, we here analyze the Lagrangian dynamics of the concentration fields. That is, we compute concentrations specific to various fluid particles as they flow through the mixing region. We first define a characteristic sample residence time $t(x)$ as an integration of the Eulerian velocity field $u(x)$ as follows

$$t(x) = \int_0^x \frac{dx'}{u(x', 0)}. \tag{11}$$

We then define the mixing time t_{mix} as the sample residence time between x-locations of mixing degree 0.1 and 0.5. Mathematically, $t_{mix} = t(x_{0.5}) - t(x_{0.1})$ where $\alpha(x_{0.5}) = 0.5$ and $\alpha(x_{0.1}) = 0.1$. Here, $x_{0.1}$ is the effective location where mixing has "started". For completeness, we also evaluated (and present in Section S6) mixing times for a near-complete mixing process defined as increase in α from 0.1 to 0.9 ($t_{0.9}$). Depending on the application, the initial sheath concentration can be relatively high compared to the initial concentration of a precious (and/or expensive) sample species. In this scenario, α values significantly less than unity may drive a reaction to completion. This prompts the definition of a third time to quantify the mixing duration; namely, the time to achieve an effective stoichiometric mixture within the sample, t_{stoich}. We quantify t_{stoich} as $t_{stoich} = t(\alpha = c_{sa,0}/c_{sh,0}) - t(\alpha = 0.1c_{sa,0}/c_{sh,0})$ for a reaction where the sample to sheath stoichiometric coefficient ratio is one. Refer to Section S8 for a discussion which shows that t_{mix}/t_{stoich} scales approximately linearly with $c_{sh,0}/c_{sa,0}$. This enables initiation of chemical reactions with a time scale that is one order of magnitude lower than t_{mix} by simply increasing the (usually inexpensive) sheath species initial concentration.

This definition of mixing time based on Lagrangian time histories among fluid particles is essential to quantify and analyze the uniformity by which reactions are initiated for the various streamlines within the sample stream. This tracking of time histories is necessary for studies which seek to use mixers to quantify chemical kinetic rates. Also, this approach to the definition and quantification of mixing time implies that mixers which achieve the thinnest characteristic stream widths are not necessarily the fastest mixers (see Hertzog et al. [5,6]). As we shall see, the thinnest sample stream does not provide the fastest mixing because the smallest sample stream diameter implies that mixing is initiated further upstream where the flow is moving slowly, and the sample stream dimensions are relatively large. For example, as we shall discuss below, in our geometry flow rate ratios of order 10^5 or higher imply that mixing is initiated inside of the center (sample stream) capillary which contains extremely slow-moving liquid. This leads to long Lagrangian mixing times which are not useful for the quantitative measurement of kinetic rates.

Lastly, we hypothesized the Lagrangian dynamics of an inlet sample streamline is a strong function of its initial location in r. For example, near-wall streamlines spend longer time within the near-

exit regions of the center capillary. However, these regions also contribute less sample fluid to the mixing region. To explore this hypothesis, we analyzed the concentration dynamics of fluid particles traveling through different and randomly seeded streamlines of the sample stream inlet. Accordingly, we define a mixing nonuniformity β as a cross-section-area-averaged standard deviation of residence times among these streamlines and normalized by the residence time of the center streamline. β is given by

$$\beta(x) = \frac{1}{t}\sqrt{\frac{\sum_j (t_j - t)^2 2\pi r_j \Delta r_j}{\pi r_{sa}^2}}. \quad (12)$$

where t and t_j are, respectively, the residence times of fluid particles traveling along the center and jth streamlines.

3. Results and discussion

3.1. Experimental model validation

Fig. 2a shows a schematic of the flow control system used to experimentally study mixing and validate the models. Fig. 2b–d shows numerical simulations (left column) and experimental (right column) hydrodynamic focusing of the sample solution into a thin stream, near the inner capillary aperture. Importantly, since the experimental images necessarily line-of-sight integrate the fluorescence signal (cf. Section S3), we here also depth-integrate the simulated sample concentration fields. That is, we applied the transform $I(x,r) \sim c_{sa}(x,r)\sqrt{r_{sa}^2 - r^2}$ to obtain fluorescence intensity images for the numerical and semi-analytical models. The values of flow rate ratio Q_{sh}/Q_{sa} in Fig. 2 were respectively 100, 1000, and 5000, while Q_{sh} was here fixed at 0.5 mL min^{-1}. The numerical simulations and experimental images are in qualitative agreement. Importantly, lower and higher Q_{sh}/Q_{sa} respectively result in wider (Fig. 2b) and narrower (Fig. 2d) sample stream widths.

Fig. 3 shows the development of the sample stream width σ along the streamwise direction x for numerical and semi-analytical model predictions, and experimental measurements. Shown are

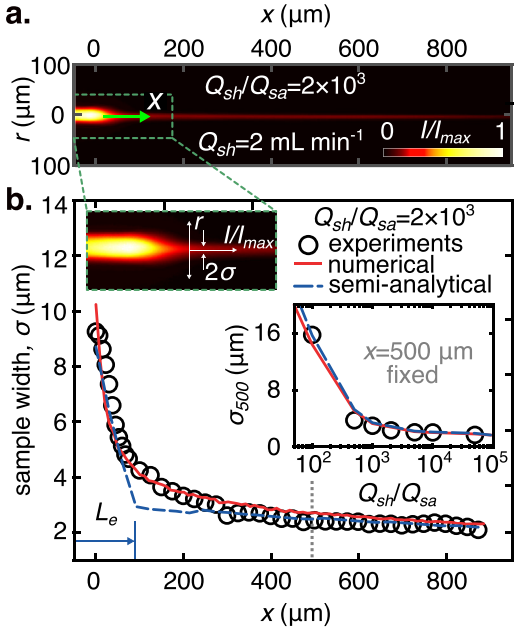

Fig. 3. (a) Epifluorescence image of hydrodynamically focused dye stream with flow rate ratio $Q_{sh}/Q_{sa} = 2000$ and $Q_{sh} = 2$ mL min^{-1}. (b) Sample width σ versus the axial position x for numerical (solid lines) and semi-analytical (dashed lines) models and experiments (open circles). Flow conditions are the same as (a). σ decreases rapidly in the first 100 μm as it is hydrodynamically focused by the faster sheath stream. The subsequent gradual decrease in the sample width is due to the taper of the middle capillary. The inset shows the sample width at $x = 500$ μm (σ_{500}) versus Q_{sh}/Q_{sa}. σ_{500} decreases sharply as Q_{sh}/Q_{sa} increases from 100 to 1000 but is less sensitive for values of Q_{sh}/Q_{sa} above about 1000.

results for $Q_{sh}/Q_{sa} = 2000$ and $Q_{sh} = 2$ mL min^{-1}. For $x < 100$ μm, σ decreased rapidly as the sample stream was accelerated by the higher velocity sheath stream. We define an "entrance length" L_e, associated with the rapid acceleration of the sample stream, as the x position after which the sample stream has been hydrodynamically focused. We hypothesize this entrance length scales as the

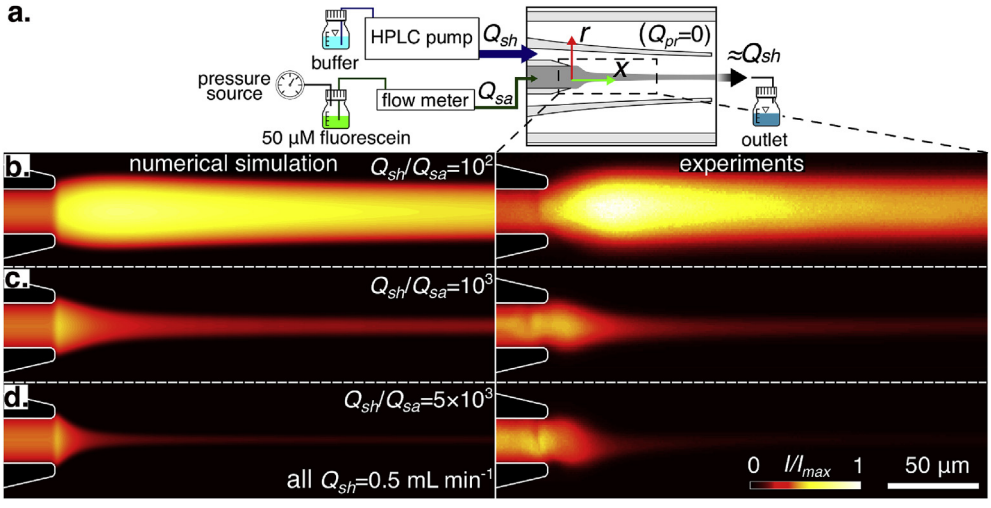

Fig. 2. (a) Schematic of experimental flow setup for hydrodynamic focusing of a fluorescent dye. (b–d) are numerical simulations (left column) and experimental (right column) images of sample concentration near the inner capillary nozzle for flow rate ratio Q_{sh}/Q_{sa} values of 100, 1000, and 5000 with fixed $Q_{sh} = 0.5$ mL min^{-1}. The numerical simulation concentration fields were depth-averaged to simulate the line-of-sight integration of the experimental optics. (b) $Q_{sh}/Q_{sa} = 100$ condition where mixing time is dominated by diffusion of sheath species into the sample stream. At the end of the middle capillary (not shown), the mixing degree $\alpha(x = L) = 0.5$, while the mixing nonuniformity $\beta(x = L) = 0.03$. (c) $Q_{sh}/Q_{sa} = 1000$ condition where $\alpha(x = L) = 0.9$ and $\beta(x = L) = 0.1$. (d) $Q_{sh}/Q_{sa} = 5000$ condition where $\alpha(x = L) = 0.9$ and $\beta(x = L) = 0.3$ at the end of the middle capillary. The sample solution contained a 50 μM solution of fluorescein and both the sample and sheath solution contained 20 mM Tris and 10 mM H–Cl buffer (measured pH = 8).

product of the Reynolds number of the sheath stream and the sheath capillary radius (cf. Section S5.2). This simplified treatment slightly under-predicts the entrance length but agrees well with the downstream region.

The inset of Fig. 3b shows the effect of flow rate ratio Q_{sh}/Q_{sa} on the sample width at $x = 500$ μm (σ_{500}). (This location is highlighted by the grey vertical dotted line in the main plot.) At this location, the sample stream radius decreased from 17 to 2 μm as Q_{sh}/Q_{sa} increased from 100 to 10^5, in agreement with our models.

3.2. Fast mixing

Fig. 4a shows a schematic of the flow control system used to quench a fluorescent dye. Fig. 4b shows experimental quenched and unquenched epifluorescence images (cf. Section 2.1.2) for flow rate ratios Q_{sh}/Q_{sa} of 500, 1000, 2000, and 5000, and fixed $Q_{sh} = 2$ mL min^{-1}. The fluorescence intensity of the sample stream is lower in the quenched images. Qualitatively, the higher Q_{sh}/Q_{sa} (e.g., 2000 and 5000) show more dramatic quenching.

Fig. 4c shows numerical and semi-analytical model intensity predictions versus x and compares these to the experimental measurements of the normalized integrated intensities for the same flow conditions as Fig. 4b. The integrated intensities were normalized by the average integrated intensity of the unquenched image within the inner capillary I_{BG}. The top and middle rows respectively show the normalized integrated intensities of the unquenched $\sum I/I_{BG}$ and quenched images $\sum I_q/I_{BG}$, while the bottom row shows their ratio $\sum I_q/\sum I$. The models and experiments are in good quantitative agreement.

$\sum I/I_{BG}$ (top row, Fig. 4c) rapidly decreases, within the initial entrance length $x < 100$ μm, to a quasi-steady value. $\sum I_q/I_{BG}$ (middle row, Fig. 4c) decreases equally rapidly within 100 μm, however, $\sum I_q/I_{BG}$ continues to decrease at a slower rate thereafter. The latter decrease in $\sum I_q/I_{BG}$ is strong evidence of the sample quenching reaction. The rate of this decrease is inversely proportional to the flow rate ratio Q_{sh}/Q_{sa}. We attribute this inverse proportionality to enhanced mixing associated with the increased upstream stretching of the sample stream for higher Q_{sh}/Q_{sa}.

Lastly, $\sum I_q/\sum I$ (bottom row, Fig. 4c) decreases from unity at $x = 0$ μm to ~0.2 at $x = 600$ μm for all values of Q_{sh}/Q_{sa}. The higher Q_{sh}/Q_{sa} conditions result in a faster decrease of the integrated intensity ratio versus x. This suggests quicker mixing occurs at higher Q_{sh}/Q_{sa} and is shown by the mixing times t_{mix} denoted in the bottom row of Fig. 4b. For example, $Q_{sh}/Q_{sa} = 500$ results in $t_{mix} = 1.2$ ms while $Q_{sh}/Q_{sa} = 5000$ results in $t_{mix} = 0.57$ ms. We attribute the small discrepancies between experiments and models (particularly for $\sum I_q/\sum I$ comparison) to the challenges of accounting for the low-level background signal associated with elastic scatter of the emitted fluorescence from the inner walls of the mixing region. This background signal levels become most important for the quenched, downstream dye whose fluorescence signal is weakest.

3.3. Parametric exploration of mixer performance

The experimentally validated numerical model was used to explore trade-offs among the three main figures of merit α, β, and t_{mix}. For this numerical study, the sample and sheath flow rates (respectively Q_{sa} and Q_{sh}) were varied over physically realizable values. Specifically, the flow rate ratio is crucial to mixing because it largely governs the radius of the non-diffuse sample stream tube radius. We show in Section S5.1 that this sample radius is negligibly affected by the sheath or sample viscosity for very large flow rate ratios. The non-diffuse sample stream radius r_{sa} is given by a mass flow balance as

$$r_{sa} = R_{sh}\sqrt{\frac{Q_{sa}}{2Q_{sh}}}. \tag{13}$$

Fig. 5a shows sheath species concentration (top row) and velocity magnitude (bottom row) fields for $Q_{sh}/Q_{sa} = 50$, 1000, and 7×10^4 with fixed $Q_{sh} = 0.5$ mL min^{-1}. Streamlines are denoted by the overlaid black lines. As expected, lower Q_{sh}/Q_{sa} (left) result in wider sample streams and consequently poorer mixing. Importantly, much higher Q_{sh}/Q_{sa} (right) eventually result in diffusion of

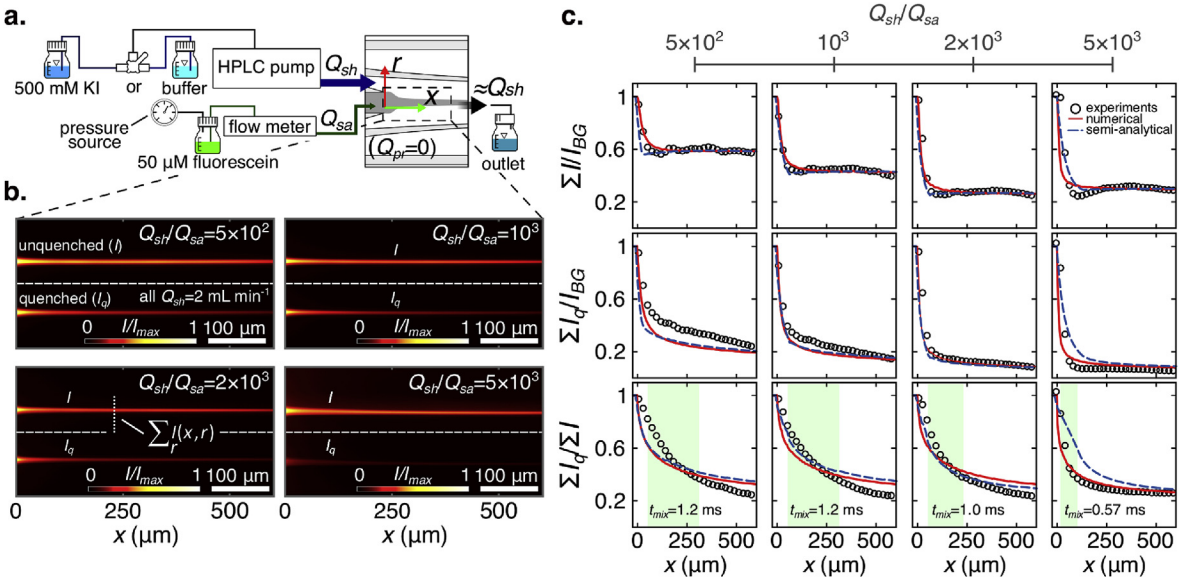

Fig. 4. (a) Schematic of experimental flow setup for hydrodynamic focusing and quenching of a fluorescent dye. (b) Epifluorescence images of unquenched and quenched dye streams for flow rate ratios Q_{sh}/Q_{sa} of 500, 1000, 2000, and 5000 with fixed $Q_{sh} = 2$ mL min^{-1}. $x = 0$ corresponds to the inner capillary aperture. (c) The top and middle rows respectively show the normalized unquenched and quenched image intensities versus x, for the same flow rate conditions as (b). The bottom row of (c) plots the ratio of the top and middle rows (i.e., quenched to unquenched intensity ratio). Results from experiments (open circles), numerical (solid lines) and semi-analytical models (dashed lines) are shown. The shaded regions in the bottom row of (c) correspond to the locations of mixing initiation and completion and the corresponding mixing times are shown.

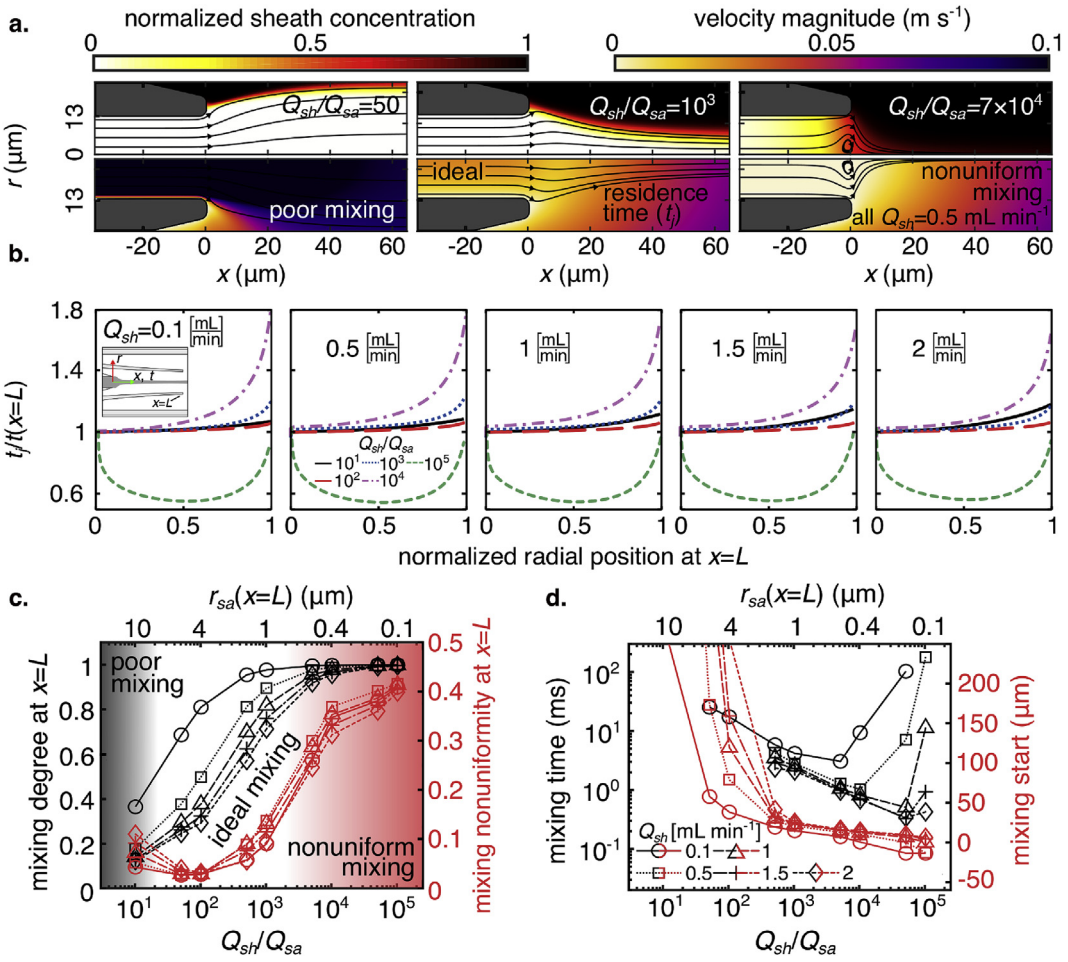

Fig. 5. (a) Numerical simulation results of normalized sheath concentration (top row) and velocity magnitude fields (bottom row) near the inner capillary region for flow rate ratios Q_{sh}/Q_{sa} of 50, 1000, and 7×10^4 with fixed $Q_{sh} = 0.5$ mL min^{-1}. The black lines with arrows represent streamlines of the flow. (b) Residence times along sample streamlines $t_j(x = L)$, normalized by the center streamline residence time $t(x = L)$ versus the streamline radial position at $r_j(x = L)$, normalized by $r_{sa}(x = L)$. Results are shown for Q_{sh}/Q_{sa} between 10 and 10^5 and for Q_{sh} between 0.1 and 2 mL min^{-1}. (c) Predicted mixing degree $\alpha(x = L)$ (black lines, left axis) and mixing nonuniformity $\beta(x = L)$ (red lines, right axis) at the middle capillary exit versus the flow rate ratio Q_{sh}/Q_{sa} and for same Q_{sh} range as (b). The mixing degree increases monotonically with Q_{sh}/Q_{sa}. The shaded regions indicate regions of either incomplete mixing (left) or nonuniform mixing (right). (d) The mixing time t_{mix} (black lines, left axis) and streamwise mixing start location $x_{0.1}$ (red lines, right axis). Nonuniform mixing at high Q_{sh}/Q_{sa} is associated with mixing initiated upstream of the inner capillary exit ($x = 0$). (For interpretation of the references to colour in this figure legend, the reader is referred to the Web version of this article.)

sheath species upstream of the inner capillary aperture. The disparate velocities near this region lead to recirculation regions including a ring vortex near the exit of the center capillary. This recirculation leads to drastically nonuniform residence times. Note this recirculation has been reported by other studies in similar flow geometries [45,46]. We hypothesize the vorticity of this vortex is generated by the no-slip condition at the inner wall of the sample tube. For overly large flow rate ratios, the sample is rapidly decelerated and advection of vorticity out of the region is limited. Both of these conditions favor formation of a vortex in this steady state flow. This vortex helps dissipate (via viscous diffusion) the sample tube vorticity.

Fig. 5b shows the residence time (cf. Section 2.4) of fluid elements which traveled along sample streamlines $t_j(x = L)$, normalized by the center streamline residence time $t(x = L)$ versus the streamline radial position at $r_j(x = L)$, normalized by $r_{sa}(x = L)$. The data is plotted for flow rate ratios Q_{sh}/Q_{sa} between 10 and 10^5 and for Q_{sh} between 0.1 and 2 mL min^{-1}. Flow rate ratios of $Q_{sh}/Q_{sa} > 10^4$ result in nonuniform residence times, while the magnitude of Q_{sh} has negligible effect. The center streamline (left edge of each plot) always provides the shortest residence time except for $Q_{sh}/Q_{sa} = 10^5$.

Fig. 5c shows the mixing degree $\alpha(x = L)$ (black symbols, left axis) versus flow rate ratio Q_{sh}/Q_{sa} for Q_{sh} between 0.1 and 2 mL min^{-1}. As indicated in the top abscissa, the non-diffuse sample stream radius $r_{sa}(x = L)$ is determined by Q_{sh}/Q_{sa} and the (fixed) geometry of the system. For $Q_{sh}/Q_{sa} < 5000$, increasing Q_{sh} results in shorter residence times and so less mixing occurs prior to the exit of the middle capillary. The mixing degree increases monotonically with the flow rate ratio and approaches unity for $Q_{sh}/Q_{sa} > 5000$. The latter trend is irrespective of Q_{sh}.

The mixing nonuniformity $\beta(x = L)$ versus Q_{sh}/Q_{sa} is also shown in Fig. 5c (red symbols, right axis) for Q_{sh} between 0.1 and 2 mL min^{-1}. The mixing nonuniformity remains below 0.1 for $10 < Q_{sh}/Q_{sa} < 1000$ but increases sharply for $Q_{sh}/Q_{sa} > 1000$. Changes in Q_{sh} have a small influence on the mixing nonuniformity, which confirms Q_{sh} primarily affects sample residence time but not mixing nonuniformity. Shaded regions indicate Q_{sh}/Q_{sa} operational regimes of incomplete mixing (left) or overly nonuniform mixing (right).

Fig. 5d shows the mixing time t_{mix} (black symbols, left axis) versus Q_{sh}/Q_{sa} for Q_{sh} between 0.1 and 2 mL min^{-1}. As described

earlier, the mixing time is defined as the time for the mixing degree to increase from 0.1 to 0.5 (i.e. $t_{mix} = t(x_{0.5}) - t(x_{0.1})$ where $\alpha(x_{0.5}) = 0.5$ and $\alpha(x_{0.1}) = 0.1$) and $x_{0.1}$ is the corresponding location of mixing start. For this definition of "mixed" ($\alpha > 0.5$), the mixer cannot achieve fully mixed flows for Q_{sh}/Q_{sa} less than about 500. The curves of t_{mix} are concave up with a local minimum mixing time. This local minimum is a trade-off between overly low Q_{sh}/Q_{sa} which requires too much radial diffusion or overly high Q_{sh}/Q_{sa} (for fixed Q_{sh}) which results in overly long times for hydrodynamic focusing. The value of the local minimum of t_{mix} varies with Q_{sh} and occurs at high values of Q_{sh}/Q_{sa}, before recirculation effects dominate ($Q_{sh}/Q_{sa} > 5 \times 10^4$). The shortest predicted mixing time t_{mix} is 350 μs for $Q_{sh}/Q_{sa} = 5 \times 10^4$ and $Q_{sh} = 2$ mL min^{-1}.

The mixing start $x_{0.1}$ versus Q_{sh}/Q_{sa} is also shown in Fig. 5d (red lines, right axis) for Q_{sh} between 0.1 and 2 mL min^{-1}. This x-location decreases monotonically with increasing Q_{sh}/Q_{sa}. Certain combinations of Q_{sh}/Q_{sa} values ($>10^4$) and Q_{sh} values (<0.5 mL min^{-1}) result in significant degrees of "pre-mixing" where overly aggressive hydrodynamic focusing results in highly nonuniform mixing initiated within the low velocity regions upstream of the sample nozzle exit (within the small inner capillary itself).

3.4. Expansion region

A unique feature of the current three-capillary mixer system is the independent control of sample width downstream of mixing and immediately prior to probing with a line-of-sight-integrating probe beam. The radial sample stream expansion increases the quantity of sample species within the path of a line-of-sight integrating probe and therefore improves detector signal-to-noise ratio (SNR). As shown in Section S9, at the exit of the mixing region ($x = L$), the sample residence time varies strongly with the sheath flow rate Q_{sh}.

Fig. 6 shows numerical simulation (left column) and experimental (right column) concentration fields of the sample stream expansion for outer flow rates Q_{pr} of −0.06, 0, and 1.2 mL min^{-1} with $Q_{sh}/Q_{sa} = 100$ and $Q_{sh} = 0.5$ mL min^{-1}. The left edge of these images corresponds to a position 200 μm downstream of the middle mixing capillary exit. Again, the line-of-sight integrations of the simulated sample concentration profiles are compared. There is good qualitative agreement between simulation and experimental concentration fields. After mixing, the combined sample and sheath stream enters the outer (third) capillary where Q_{pr} can be controlled to independently tune deceleration of the flow. As shown in Fig. 6b, a flow in the opposite direction of the sample stream (towards the left direction) achieved a 14-fold expansion of the sample stream radius. The flow conditions in Fig. 6b–d all had effective sample stream radii σ of 4 μm (at the end of the middle capillary) and produced expanded radii of respectively 50, 40, and 9 μm. The time scale of these expansions can be characterized by the sample residence time from the exit of the middle capillary to the location where the radius of the diffusive sample stream reaches 90% of its maximum value. The latter cases result in expansion times of 8, 5, and 1 ms, respectively. This expansion process is suitable for higher SNR detection using, for example, detection beams of order 100 μm full-width at half-maximum.

4. Conclusions

We have developed a novel microfluidic device which achieves rapid and uniform mixing, as well as improved detection signal-to-noise ratio downstream. The device employs a three-capillary design wherein a sample stream is hydrodynamically focused and subsequently rapidly expanded. Numerical and semi-analytical models were developed and validated using fluorescein-iodide dye visualization and quenching experiments. Further, these models were used to parametrically explore the operational space of the device. To our knowledge, this work is the first to quantitatively demonstrate both highly uniform mixing and a mixing time (t_{mix}, as described in Section 2.4) on the order of 100 μs. Unlike previous work in rapid 3D mixers, we present a quantitative, detailed study of the trade-offs between a bulk mixing time scale (e.g. t_{mix}) and the nonuniformity of mixing, as quantified by the width of fluid particle residence times. As might be expected, higher values of Q_{sh}/Q_{sa} promote faster mixing (e.g. smaller t_{mix}). However, in this geometry, values of Q_{sh}/Q_{sa} higher than a critical value of about 10^4 lead to a pronounced recirculation region in the form of a ring vortex near the aperture of the inner capillary. Streamline curvature near this recirculation causes a rapid broadening of the residence times for fluid particles flowing through the

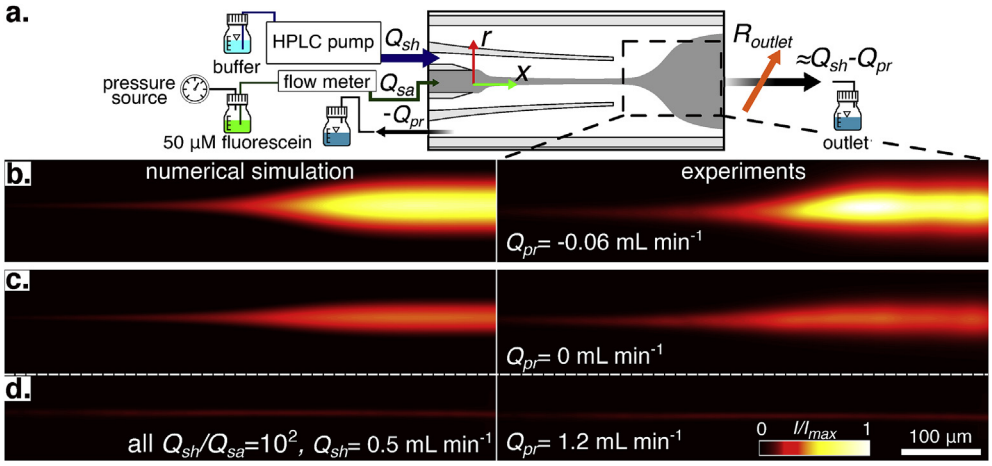

Fig. 6. (a) Schematic of experimental flow setup for post-mixing expansion of a fluorescent dye with a negative probe flow rate Q_{pr} (as in (b)). For $Q_{pr} > 0$ (as in (c)) a secondary HPLC pump was used. For $Q_{pr} = 0$ (as in (d)) the outer capillary inlet was sealed. (b–d) are numerical simulations (left column) and experimental (right column) images of sample concentration near the inner capillary nozzle for Q_{pr} of −0.06, 0, and 1.2 mL min^{-1} and fixed $Q_{sh}/Q_{sa} = 100$ and $Q_{sh} = 0.5$ mL min^{-1}. The left edge of these images corresponds to a position 200 μm downstream of the middle mixing capillary exit (see (a)). The simulated concentration fields were depth-averaged to recreate the line-of-sight integration of experimental images. The flow conditions in (a–c) all had effective, experimentally measured sample width $\sigma = 4$ μm (at the end of the middle capillary) and resulted in expanded width σ of respectively 50, 40, and 9 μm. The expansion times (the Lagrangian time for a fluid particle starting from the exit of the middle capillary to the location where σ reaches 90% of its final value) are respectively 8, 5, and 1 ms.

mixer, leading to nonuniform mixing. We further demonstrated a post-mixing, 14-fold expansion of the radius of the mixed stream.

The models suggest that the flow rate ratio regime of about ~1000 to ~5000 provides a high mixing degree and uniformity for sheath flow rates of 0.1–2 mL min^{-1}. The quantitative analysis of the current mixer is applicable to the design of a wide variety of microfluidic mixers aimed at studies of fast chemical reactions, particularly those with detectors with line-of-sight integration.

Declaration of competing interest

The authors declare that they have no known competing financial interests or personal relationships that could have appeared to influence the work reported in this paper.

CRediT authorship contribution statement

Diego A. Huyke: Investigation, Methodology, Formal analysis, Writing - original draft. **Ashwin Ramachandran:** Investigation, Methodology, Writing - original draft. **Diego I. Oyarzun:** Visualization, Writing - original draft. **Thomas Kroll:** Investigation, Writing - original draft, Funding acquisition. **Daniel P. DePonte:** Investigation, Writing - original draft, Funding acquisition, Conceptualization, Project administration. **Juan G. Santiago:** Investigation, Methodology, Writing - original draft.

Acknowledgements

D.A.H. is supported by a National Science Foundation Graduate Research Fellowship and would like to thank Nathan Degraaff for his contributions. A.R. gratefully acknowledges support from the BioX Bowes Fellowship of Stanford University. Use of the Stanford Synchrotron Radiation Lightsource and the Linac Coherent Light Source, SLAC National Accelerator Laboratory, is supported by the U.S. Department of Energy, Office of Science, Office of Basic Energy Sciences under Contract No. DE-AC02-76SF00515. The SSRL Structural Molecular Biology Program is supported by the DOE Office of Biological and Environmental Research, and by the National Institutes of Health, National Institute of General Medical Sciences (including P41GM103393). The contents of this publication are solely the responsibility of the authors and do not necessarily represent the official views of NIGMS or NIH.

Appendix A. Supplementary data

Supplementary data to this article can be found online at https://doi.org/10.1016/j.aca.2020.01.013.

References

[1] C.-K. Chan, Y. Hu, S. Takahashi, D.L. Rousseau, W.A. Eaton, J. Hofrichter, Submillisecond protein folding kinetics studied by ultrarapid mixing, Proc. Natl. Acad. Sci. 94 (1997) 1779–1784.
[2] W.A. Eaton, V. Muñoz, S.J. Hagen, G.S. Jas, L.J. Lapidus, E.R. Henry, J. Hofrichter, Fast kinetics and mechanisms in protein folding, Annu. Rev. Biophys. Biomol. Struct. 29 (2000) 327–359.
[3] E.A. Lipman, B. Schuler, O. Bakajin, W.A. Eaton, Single-Molecule measurement of protein folding kinetics, Science (80-.) 301 (2003) 1233–1235.
[4] H. Roder, K. Maki, H. Cheng, M.C. Ramachandra Shastry, Rapid mixing methods for exploring the kinetics of protein folding, Methods 34 (2004) 15–27.
[5] D.E. Hertzog, X. Michalet, M. Jäger, X. Kong, J.G. Santiago, S. Weiss, O. Bakajin, Femtomole mixer for microsecond kinetic studies of protein folding, Anal. Chem. 76 (2004) 7169–7178.
[6] D.E. Hertzog, B. Ivorra, B. Mohammadi, O. Bakajin, J.G. Santiago, Optimization of a microfluidic mixer for studying protein folding kinetics, Anal. Chem. 78 (2006) 4299–4306.
[7] B. Wunderlich, D. Nettels, S. Benke, J. Clark, S. Weidner, H. Hofmann, S.H. Pfeil, B. Schuler, Microfluidic mixer designed for performing single-molecule kinetics with confocal detection on timescales from milliseconds to minutes, Nat. Protoc. 8 (2013) 1459–1474.
[8] G.H. Seong, R.M. Crooks, Efficient mixing and reactions within microfluidic channels using microbead-supported catalysts, J. Am. Chem. Soc. 124 (2002) 13360–13361.
[9] M.R. Bringer, C.J. Gerdts, H. Song, J.D. Tice, R.F. Ismagilov, Microfluidic systems for chemical kinetics that rely on chaotic mixing in droplets, Philos. Trans. R. Soc. London. Ser. A Math. Phys. Eng. Sci. 362 (2004) 1087–1104.
[10] Y. Asanomi, H. Yamaguchi, M. Miyazaki, H. Maeda, Enzyme-immobilized microfluidic process reactors, Molecules 16 (2011) 6041–6059.
[11] C. Beta, E. Bodenschatz, Microfluidic tools for quantitative studies of eukaryotic chemotaxis, Eur. J. Cell Biol. 90 (2011) 811–816.
[12] M.C. Liu, Y.-C. Tai, A 3-D microfluidic combinatorial cell array, Biomed. Microdevices 13 (2011) 191–201.
[13] W.G. Lee, Y.-G. Kim, B.G. Chung, U. Demirci, A. Khademhosseini, Nano/Microfluidics for diagnosis of infectious diseases in developing countries, Adv. Drug Deliv. Rev. 62 (2010) 449–457.
[14] W. Jing, W. Zhao, S. Liu, L. Li, C.-T. Tsai, X. Fan, W. Wu, J. Li, X. Yang, G. Sui, Microfluidic device for efficient airborne bacteria capture and enrichment, Anal. Chem. 85 (2013) 5255–5262.
[15] S.T. Sanjay, G. Fu, M. Dou, F. Xu, R. Liu, H. Qi, X. Li, Biomarker detection for disease diagnosis using cost-effective microfluidic platforms, Analyst 140 (2015) 7062–7081.
[16] H.S.M. Ali, P. York, N. Blagden, Preparation of hydrocortisone nanosuspension through a bottom-up nanoprecipitation technique using microfluidic reactors, Int. J. Pharm. 375 (2009) 107–113.
[17] J.Y. Kim, D. Taylor, K. Rege, H.S. Kim, A.R. Han, A. Jayaraman, Novel high-throughput screening system for cancer therapy with simultaneous combination treatments, MicroTAS (2010) 836–838, 2010.
[18] D. An, K. Kim, J. Kim, Microfluidic system based high throughput drug screening system for curcumin/TRAIL combinational chemotherapy in human prostate cancer PC3 cells, Biomol. Ther. (Seoul). 22 (2014) 355–362.
[19] S. Kwakye, A. Baeumner, A microfluidic biosensor based on nucleic acid sequence recognition, Anal. Bioanal. Chem. 376 (2003) 1062–1068.
[20] W.C. Hui, L. Yobas, V.D. Samper, C.-K. Heng, S. Liw, H. Ji, Y. Chen, L. Cong, J. Li, T.M. Lim, Microfluidic systems for extracting nucleic acids for DNA and RNA analysis, Sensors Actuators A Phys 133 (2007) 335–339.
[21] S.R. Nugen, P.J. Asiello, J.T. Connelly, A.J. Baeumner, PMMA biosensor for nucleic acids with integrated mixer and electrochemical detection, Biosens. Bioelectron. 24 (2009) 2428–2433.
[22] J.B. Knight, A. Vishwanath, J.P. Brody, R.H. Austin, Hydrodynamic focusing on a silicon chip: mixing nanoliters in microseconds, Phys. Rev. Lett. 80 (1998) 3863–3866.
[23] H.Y. Park, X. Qiu, E. Rhoades, J. Korlach, L.W. Kwok, W.R. Zipfel, W.W. Webb, L. Pollack, Achieving uniform mixing in a microfluidic device: hydrodynamic focusing prior to mixing, Anal. Chem. 78 (2006) 4465–4473.
[24] K.S. Burke, D. Parul, M.J. Reddish, R.B. Dyer, A simple three-dimensional-focusing, continuous-flow mixer for the study of fast protein dynamics, Lab Chip 13 (2013) 2912.
[25] A. Plumridge, A.M. Katz, G.D. Calvey, R. Elber, S. Kirmizialtin, L. Pollack, Revealing the distinct folding phases of an RNA three-helix junction, Nucleic Acids Res. 46 (2018) 7354–7365.
[26] D.A. Huyke, A. Ramachandran, T. Kroll, D.P. DePonte, J.G. Santiago, Fast and homogenous mixing in a coaxial capillary device with two sheath flow, in: DFD19 Meet. Am. Phys. Soc. Fast, Bulletin of the American Physical Society, 2019.
[27] D. Wang, U. Weierstall, L. Pollack, J. Spence, Double-focusing mixing jet for XFEL study of chemical kinetics, J. Synchrotron Radiat. 21 (2014) 1364–1366.
[28] G.D. Calvey, A.M. Katz, C.B. Schaffer, L. Pollack, Mixing injector enables time-resolved crystallography with high hit rate at X-ray free electron lasers, Struct. Dyn. 3 (2016), 054301.
[29] D. Oberthuer, J. Knoška, M.O. Wiedorn, K.R. Beyerlein, D.A. Bushnell, E.G. Kovaleva, M. Heymann, L. Gumprecht, R.A. Kirian, A. Barty, V. Mariani, A. Tolstikova, L. Adriano, S. Awel, M. Barthelmess, K. Dörner, P.L. Xavier, O. Yefanov, D.R. James, G. Nelson, D. Wang, G. Calvey, Y. Chen, A. Schmidt, M. Szczepek, S. Frielingsdorf, O. Lenz, E. Snell, P.J. Robinson, B. Šarler, G. Belšak, M. Maček, F. Wilde, A. Aquila, S. Boutet, M. Liang, M.S. Hunter, P. Scheerer, J.D. Lipscomb, U. Weierstall, R.D. Kornberg, J.C.H. Spence, L. Pollack, H.N. Chapman, S. Bajt, Double-flow focused liquid injector for efficient serial femtosecond crystallography, Sci. Rep. 7 (2017) 46846.
[30] G.D. Calvey, A.M. Katz, L. Pollack, Microfluidic mixing injector holder enables routine structural enzymology measurements with mix-and-inject serial crystallography using X-ray free electron lasers, Anal. Chem. 91 (2019) 7139–7144.
[31] H. Liao, P.K. Dasgupta, K. Srinivasan, Y. Liu, Mixing characteristics of mixers in flow analysis. Application to two-dimensional detection in ion chromatography, Anal. Chem. 87 (2015) 793–800.
[32] L.D. Scampavia, G. Blankenstein, J. Ruzicka, G.D. Christian, A coaxial jet mixer for rapid kinetic analysis in flow injection and flow injection cytometry, Anal. Chem. 67 (1995) 2743–2749.
[33] K.M. Hamadani, S. Weiss, Nonequilibrium single molecule protein folding in a coaxial mixer, Biophys. J. 95 (2008) 352–365.
[34] S.A. Pabit, S.J. Hagen, Laminar-flow fluid mixer for fast fluorescence kinetics studies, Biophys. J. 83 (2002) 2872–2878.
[35] E.M. Chan, M.A. Marcus, S. Fakra, M. ElNaggar, R.A. Mathies, A.P. Alivisatos,

Millisecond kinetics of nanocrystal cation exchange using microfluidic X-ray absorption spectroscopy †, J. Phys. Chem. A 111 (2007) 12210–12215.
[36] H. Chen, Y. Zhao, J. Li, M. Guo, J. Wan, D.A. Weitz, H.A. Stone, Reactions in double emulsions by flow-controlled coalescence of encapsulated drops, Lab Chip 11 (2011) 2312.
[37] S. Bohne, M. Heymann, H.N. Chapman, H.K. Trieu, S. Bajt, 3D printed nozzles on a silicon fluidic chip, Rev. Sci. Instrum. 90 (2019).
[38] Y. Bellouard, A. Champion, B. Lenssen, M. Matteucci, A. Schaap, M. Beresna, C. Corbari, M. Gecevičius, P. Kazansky, O. Chappuis, M. Kral, R. Clavel, F. Barrot, J.M. Breguet, Y. Mabillard, S. Bottinelli, M. Hopper, C. Hoenninger, E. Mottay, J. Lopez, The Femtoprint project, J. Laser Micro Nanoeng. 7 (2012) 1–10.
[39] C. Culbertson, Diffusion coefficient measurements in microfluidic devices, Talanta 56 (2002) 365–373.
[40] P.M. Wheat, J.D. Posner, Quantifying mixing using equilibrium reactions, Phys. Fluids 21 (2009), 037101.
[41] F.M. White, Viscous Fluid Flow, third ed., McGraw-Hill, Singapore, 2006.
[42] J. Crank, The Mathematics of Diffusion, Oxford University Press, 1975.
[43] D. Ahmed, X. Mao, J. Shi, B.K. Juluri, T.J. Huang, A millisecond micromixer via single-bubble-based acoustic streaming, Lab Chip 9 (2009) 2738.
[44] A.N. Hellman, K.R. Rau, H.H. Yoon, S. Bae, J.F. Palmer, K.S. Phillips, N.L. Allbritton, V. Venugopalan, Laser-induced mixing in microfluidic channels, Anal. Chem. 79 (2007) 4484–4492.
[45] I.R. Damian, S. Hardt, C. Balan, From flow focusing to vortex formation in crossing microchannels, Microfluid, Nanofluidics 21 (2017) 142.
[46] A. Borgogna, M.A. Murmura, M.C. Annesini, M. Giona, S. Cerbelli, Inertia-driven enhancement of mixing efficiency in microfluidic cross-junctions: a combined Eulerian/Lagrangian approach, Microfluid. Nanofluidics 22 (2018) 1–15.

Supporting Information for

On the competition between mixing rate and uniformity in a coaxial hydrodynamic focusing mixer

Diego A. Huyke[a], Ashwin Ramachandran[b], Diego I. Oyarzun[a], Thomas Kroll[c], Daniel P. DePonte[c], Juan G. Santiago[a,*]

[a] *Department of Mechanical Engineering, Stanford University, Stanford, CA 94305, USA*

[b] *Department of Aeronautics & Astronautics, Stanford University, Stanford, CA 94305, USA*

[c] *SLAC National Accelerator Laboratory, Menlo Park, CA 94025, USA*

[*] To whom correspondence should be addressed. E-mail: juan.santiago@stanford.edu

This document provides additional information regarding the experimental setup, calibration of the dye and quencher reaction, numerical and semi-analytical models, varied definitions of mixing times, and sample residence times. Also provided are details of a mixer version which employs a polyimide outer capillary (more easily applicable to hard X-ray spectroscopy studies).

Contents

S1. Performance comparison of various 3D hydrodynamic mixers

To our knowledge, our work is the first 3D hydrodynamic focusing mixer study to define "mixing time" based on a Lagrangian residence time required for a sample fluid element to transition between two fixed values of sheath-species concentration. As described in Section 2.4 of the current paper, we chose the residence time between mixing degrees, α, of 0.1 and 0.5 as a rational and quantitative measure of mixing time.

Published studies of 3D hydrodynamic focusing mixers have used a variety of other mixing time definitions. Perhaps the most common measure is a time interval used in quenched fluorescence experiments (typically iodide quenching of fluorescein) that we here term a kinematic quenching time. The latter is defined as the residence time experienced by a sample fluid particle between the exit of the sample nozzle/outlet and a point where the fluorescence is quenched to a certain degree, e.g. to 50% of the steady-state, quenched value. We do not advocate this measure as it neglects any "premixing" that may occur upstream of the sample nozzle outlet. This premixing is associated with overly high sheath-to-sample flow rate ratios and relatively slow moving sample in the sample nozzle that leads to diffusion of sheath species upstream and into the sample nozzle. Hence, this type of mixing time definition drives designers to overly aggressive focusing of the sample stream. Such focusing decreases sample stream width but eventually increase mixing time.

Table S1. Summary of performance comparison across mixing devices. Shown in the table are brief descriptions of mixers, the target applications, the Lagrangian mixing times (as per the current paper), the aforementioned kinematic quench times, the concentration of quenchers (which also influences quenching dynamics), and the sample stream tube radii at the location where the sample stream is quenched to 50% of the steady state value.

Mixer design	Application	Lagrangian mixing time† (μs)	Kinematic quench time* (μs)	Quencher concentration (mM)	Sample stream tube radius‡ (μm)
Coaxial round and square capillaries [1]	UV fluorescence spectroscopy	-	560	1.5	-
Coaxial round and square capillaries [2]	Single molecule fluorescence resonance energy transfer	-	-	-	2.3
Coaxial round capillaries [3]	UV fluorescence spectroscopy	590	178	2500	1.1
Coaxial round capillaries with "mixing section" [4]	X-ray serial femtosecond crystallography	760	~350	300	2.8
Coaxial round capillaries with "mixing section" (current paper)	X-ray absorption/emission spectroscopy	570	320	500	2.0

† This the mixing time based on the sheath-species concentrations experienced by a sample fluid element as it passes through the mixer (cf. Section 2.4 of the current paper).

* We do not recommend this mixing time definition as it ignores any premixing that may occur at high sheath-to-sample flow rate ratios. Such conditions can cause sheath species to diffuse upstream into the sample nozzle.

‡ Sample stream tube radius at the location where the sample stream is quenched to 50% of the steady state value.

We next provide a few notes regarding Table S1. For the Pabit et al. [1] reference, we used their highest sheath-to-sample flow rate condition (which was their reported best mixing performance). Hamadani et al. [2] used single molecule fluorescence resonance energy transfer and a 3D hydrodynamic focusing mixer. The latter paper reported insufficient details for us to quantify mixing time and so we report only the focused stream tube radius (their mixer had no taper after hydrodynamic focusing).

Next, Burke et al. [3] reported a type of kinematic quench time which assumes that the velocity of the center sample streamline is accelerated instantaneously to twice the bulk velocity of the mixed

streams. This treatment is inaccurate as it ignores the acceleration region during hydrodynamic focusing (i.e. the finite "entrance length" associated with developing the flow). For our estimate in Table S2, we computed the residence time for this development length using a numerical simulation of the Burke geometry, flow conditions, and the diffusivity of the sheath species using COMSOL Multiphysics 5.4 (COMSOL, Sweden). This simulation also enabled us to estimate a Lagrangian mixing time (as defined in the current work).

Calvey et al. [4] reported a "premixing time" of about 100 µs. This is the residence time of a fluid particle in the aforementioned development region between the sample nozzle exit area and the region where the sample has been hydrodynamically focused (prior to the taper of the Calvey mixer). Calvey et al. also reported a time from the point after this development for fluorescence quenching. We therefore added this "premixing time" and the reported 250 µs time after acceleration for a fair comparison to the other mixers. Further, as with the Burke mixer, we also simulated the geometry and flow conditions of Calvey et al. in COMSOL to estimate the Lagrangian mixing time.

Again, we stress that our work clearly shows that significant mixing can occur within the initial acceleration region of the hydrodynamic focusing (see Section 3.3 and Figure 5 of the current paper). Significant mixing can occur even within the sample nozzle tube (upstream of the sample nozzle outlet)—an effect ignored by such "kinematic quench times".

S2. Detailed device fabrication, assembly, and operation

Figure S1 shows the fabrication process of the mixer components. First, the mixer capillaries were fashioned from fused silica (FSC) and borosilicate glass (GC) with modifications to the capillary ends. A spacer was additionally machined to center the FSC within the GC and yet allow flow through this annular space. The spacer was laser cut from a 125 µm thick polyimide sheet and is shown in Figure S1 (see Calvey et al. [4] for a similar spacer design). In the final fabrication step, a computer numerical control (CNC) mill produced an acrylic mixer holder (see Figure S2a) which interfaced with the mixer and experimental setup.

Figure S2 shows the final assembled mixer. In the assembly process, a microfluidic tee junction (PEEK tee, IDEX, USA) secured each capillary in place and was used to provide fluid flow into or out of the device. Next, the inner, middle, and outer capillary were telescoped and finally the tee junctions were secured against the aforementioned acrylic holder. Figure S3 shows the positive (in the main flow direction) and negative outer capillary flow configuration controls.

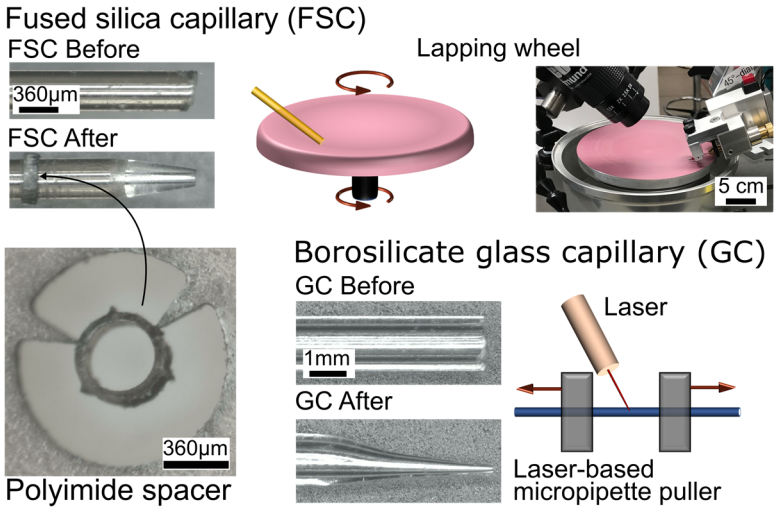

Figure S1. Schematic fabrication of mixer components. Fabrication commences with a fused silica capillary (FSC, 13 µm inner radius (IR) and 180 µm outer radius (OR), Molex, USA) and a borosilicate glass capillary (GC, 250 µm IR and 500 µm OR, Sutter Instrument, USA). The former of these is modified by grinding one end against a precision lapping wheel to produce a sharpened-pencil-like nozzle. In turn, the latter of these is pulled using a using a patch pipette technique pulling device (P-2000, Sutter Instrument, USA). The pulling process was used to produce GC tapers ~3 mm in length with a tip inner radius, R_{sa}, of 50 µm. The polyimide spacer shown on the bottom left was laser cut from 125 µm thick polyimide sheet. This spacer press-fit onto the outer surface of the FSC prior to assembly and was placed approximately 2 mm from the tip of the FSC.

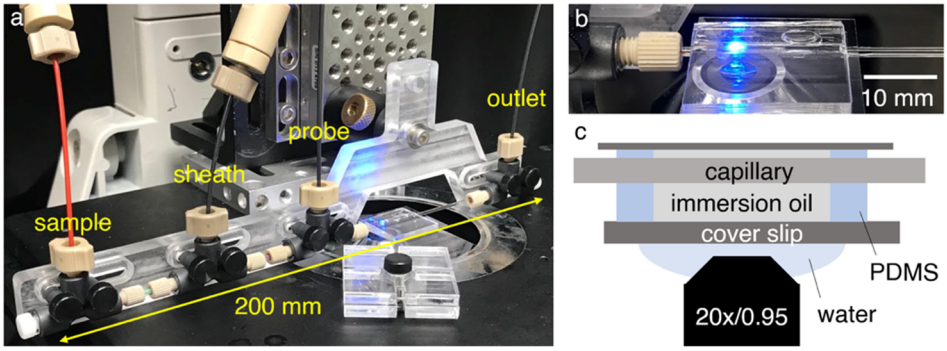

Figure S2. (a) Three capillary mixer system mounted on acrylic holder and imaged on inverted microscope. Image (b) and schematic (c) of index-matching immersion oil and Polydimethylsiloxane (PDMS) construction used to eliminate optical effects associated with the round capillary of the mixer. For imaging of flows on a conventional widefield microscope, we threaded a PDMS and cover slip glass subassembly through the outer capillary. This PDMS-glass subassembly was flooded with microscope immersion oil (refractive index $n = 1.333$) and used to reduce optical distortion associated with the curved surface of the capillary wall.

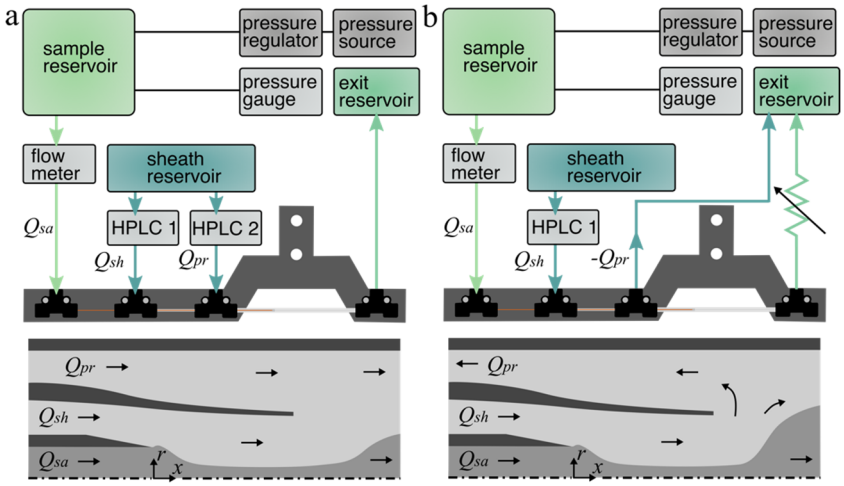

Figure S3. Schematic showing positive (a) and negative (b) flow rates into the upstream connection of the third (outer) capillary. Depending on the desired degree of flow deceleration, flow was drive into (for less expansion) or out of (for more expansion) the left-hand-side of the outermost capillary, respectively. An HPLC pump (LC-20AD, Shimadzu Corp., Japan) provided flow into this connection of the outer capillary. Conversely, a microfluidic backpressure regulator (Micro-splitter valve, IDEX Corp., USA) at the main outlet divided the flow between both outer capillary connections. The ratio of the hydraulic resistances of the outer capillary connections determined the volumetric withdrawal rate out of each connection. Lastly, a liquid flow meter with an accuracy of 0.15% (Flow Meter Standard, CorSolutions, LLC, USA) measured the flow rate out of the left connection of the outer capillary.

S3. Fluorescence intensity image processing

The mixer geometry limits microscope objective selection to those with working distances larger than the outer radius of the outer capillaries. These outer radii are here 750 μm for the outermost borosilicate capillary and 350 μm for the polyimide capillary version described in Section S10. This optical access limits the numerical aperture of the objective to a maximum of about 0.95. Further, the sample stream radii are, after the initial rapid focusing by the sheath flow, order one micron (or less). The visualization reported here uses epifluorescence with a 20x/0.95 water immersion objective (MRD77200, Nikon, Japan). The depth of field δz of these images can be approximated as

$$\delta z = \frac{n\lambda}{2NA^2} + \frac{n}{7}\frac{1000}{NA \cdot M}, \tag{1}$$

where n is the refractive index of the fluid between the mixer and the objective (here 1.333), λ is the wavelength of light, NA is the objective numerical aperture, and M is the objective magnification [5]. This results in $z = 11\mu\text{m}$ for the objective used here. The aforementioned experimental constraints imply that the depth of field of the imaging are a line-of-sight integration of the intensity field of the sample stream.

For calibration of the dye quencher rate coefficient, a straight channel chip with width 1 mm, depth 0.2 mm and length 59 mm (Fluidic 138, ChipShop, USA) was flooded and imaged with fixed dye and varied quencher concentrations. Fluorescein (Sigma-Aldrich, USA) was chosen as the dye with a fixed concentration of 50 μM, while the concentration of potassium iodide was varied from 0 to 500 mM. All solutions were mixed into 20 mM Tris and 10 mM H-Cl buffer with a measured $\text{pH} = 8$. Images were acquired using the microscope, filter cube, and camera setup described in the current paper, along with a 10x/0.45 air immersion objective (Nikon, Japan). Figure S4 shows a calibration plot of measured values of the light intensity ratio of fluorescein versus potassium iodide concentration. The curve was used to convert the measured light ratio from the mixing experiments to salt concentration. The conversion is given by

$$c_{I^-} = \frac{1}{K_{SV}}\left[\left(\frac{\sum_r I_q}{\sum_r I}\right)^{-1} - 1\right], \tag{2}$$

where c_{I^-} is the concentration of iodide and K_{SV} is the quencher rate coefficient (measured to be 7.29 M^{-1}). Equation 2 was also used to calculate the integrated intensity ratio of the numerical and semi-analytical simulations.

The time scale τ of the fluorescein-iodide quenching reaction can be estimated from the Stern-Volmer theory for collisional quenching as [6]

$$\tau = \frac{\tau_0}{1 + K_{SV} c_{I^-}}, \tag{3}$$

where τ_0 is the excited state lifetime of fluorescein in the absence of the quencher (iodide), and K_{SV} is the Stern-Volmer quenching constant (see Figure S4). For our conditions, $K_{SV} = 7.29\ \text{M}^{-1}$

and $\tau_0 \approx$ 4 ns [7], and $c_{I^-} = 0.5\,\mathrm{M}$, and we estimate the time scale of the quenching reaction τ ≈0.9 ns. We advocate that such a fast reaction is the "gold standard" to quantify mixing performance. See for example Knight et al. [8], Pabit et al. [1], and Hertzog et al. [9,10].

Figure S5 shows typical fluorescence intensity images unquenched (top) and quenched dye streams (bottom) near the inner capillary exit area. We define the fluorescence intensity ratio as $\sum_r I_q / \sum_r I$. Here I_q is the measured (line-of-sight-integrated) fluorescence intensity of the quenched experiment image and I is the measured fluorescence intensity of the unquenched experiment images. The two images are registered by aligning the inner capillary tip at $x = 0$.

Figure S6 is analogous to the bottom row of Figure 4c in the current paper, but shows numerical and semi-analytical model predictions of the cross-section-area-averaged concentration of iodide versus x and compares these to experimental measurements. Shown is data for flow rate ratios Q_{sh} / Q_{sa} of 5×10^2, 10^3, 2×10^3, and 5×10^3 with fixed $Q_{sh} = 2\,\mathrm{mL\ min^{-1}}$.

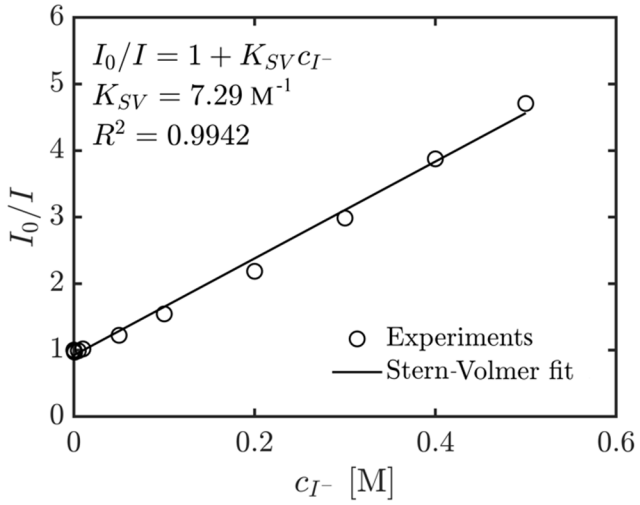

Figure S4. Calibration curve from stopped flow experiments. Open circles indicate intensity ratio measured with from stopped-flow mixing experiments. Solid line is fit to Stern-Volmer equation, given by $I_0 / I = 1 + K_{SV} c_{I^-}$. The measured quenched rate coefficient was $K_{SV} = 7.29\,\mathrm{M}^{-1}$. This calibration was used to calculate salt concentrations in quenching experiments.

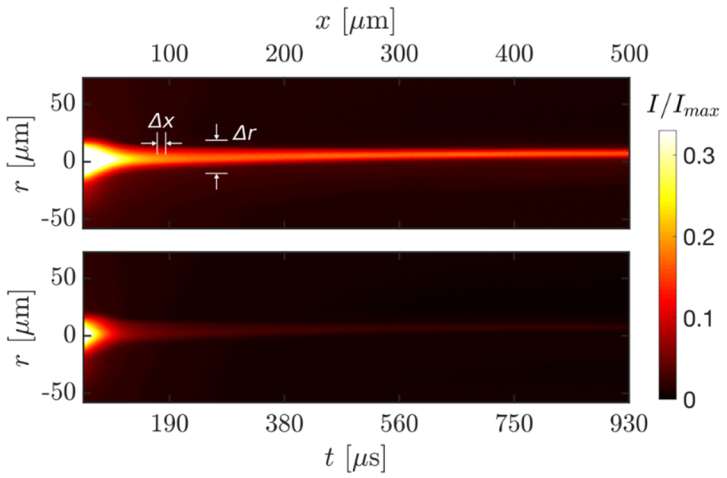

Figure S5. Experimental fluorescence intensity images of unquenched (top) and quenched (bottom) dye streams. The experimental conditions were $Q_{sh}/Q_{sa}=5000$ and $Q_{sh}=30\,\mu\text{L s}^{-1}$. All images were processed with a flat-field image correction technique [11] before extraction of concentration data. To quantify net quenching, pixels were first averaged along the streamwise direction, corresponding to superpixels of Δx=10 μm (equivalent to 30 pixels). Subsequently, the image processing script summed image intensities along the r (vertical) direction to obtain the integrated intensity for each superpixel column. Images were taken on an inverted microscope (Eclipse TE 300E, Nikon, Japan) equipped with a 20x/0.95 objective (MRD77200, Nikon, Japan).

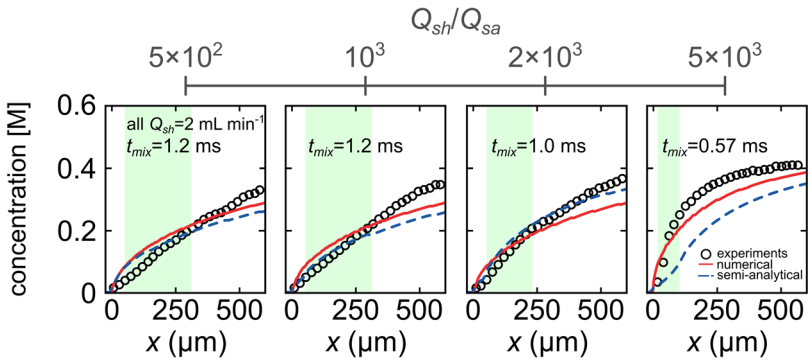

Figure S6. Numerical (solid lines) and semi-analytical (dashed lines) model predictions of the cross-section-area-averaged concentration of iodide versus x compared to experimental measurements (open circles). Shown is data for flow rate ratios Q_{sh}/Q_{sa} of 5×10^2, 10^3, 2×10^3, and 5×10^3 with fixed $Q_{sh}=2\,\text{mL min}^{-1}$. The shaded regions correspond to the locations of mixing initiation and completion and the corresponding mixing times are shown. The predicted iodide concentration (from simulations) and the Stern-Volmer equation were used to predict the integrated intensity ratio.

S4. Numerical model mesh distribution and grid independence study

Here we summarize a mesh distribution and grid independence study of our numerical model. The model was used to obtain solutions to the steady-state, incompressible Navier-Stokes and convection-diffusion equations, and it was implemented in COMSOL Multiphysics 5.4 (COMSOL, Sweden).

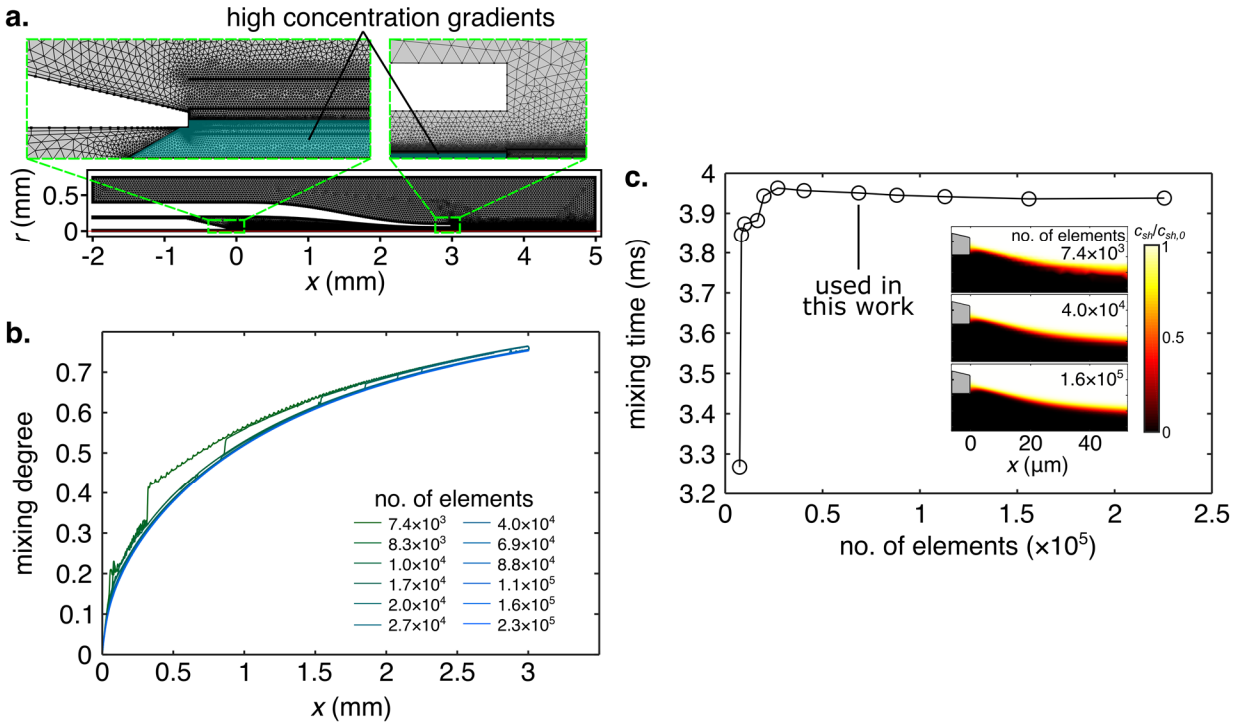

Figure S7. Mesh distribution (a) of axisymmetric numerical model of coaxial capillary mixer. 2D tetra elements almost fully cover the computational domain, except for regions near walls which are covered by 2D hexahedral meshes. Shown are the inner, middle, and outermost capillary regions. The regions highlighted in light blue correspond to regions of expected high velocity and concentration gradients. Thus, the mesh density in these regions was increased. The mixing degree versus x for increasing number of mesh elements inside of the high- -gradient region is shown in (b). Here, Q_{sh}/Q_{sa} and $Q_{sh} = 1.0\,\text{mL min}^{-1}$. The values of mixing degree converge as the number of mesh elements was increased from 7.4 × 10^3 to 2.3 × 10^5. The time to mix versus number of mesh elements inside of the high- -gradient region is shown in (c). The time to mix is independent of the grid size for more than ~4 × 10^4 mesh elements.

S5. Semi-analytical convection-diffusion model of species transport

This section describes the semi-analytical model. First, a momentum balance yields an expression for the radius of the fully developed (non-diffuse) sample stream tube $r_{sa} = r_{sa}(x)$ (see Figure 1a of current paper). Next, an estimated sample stream entrance length L_e is used to correct for $r_{sa}(x < L_e)$. Finally, given appropriate boundary and initial conditions, the model considers the diffusion of species (sample and sheath) within small streamwise sections of the flow as radial diffusion within a cylinder at the local inner radius of the tapered middle capillary.

S5.1 Derivation of sample stream radius. To derive an expression for r_{sa} as a function of x, the model assumes the flow is laminar, steady, and axisymmetric about the x axis. The model further assumes there are no radial or azimuthal velocity components, and that, downstream of the entrance region, each section of the coaxial flow within the tapered middle capillary is locally fully developed. Under these assumptions, the conservation of momentum equations in the x- and r-directions for the sample and sheath streams are

$$\frac{1}{r}\frac{\partial}{\partial r}\left(r\frac{\partial u_{sa}}{\partial r}\right) = \frac{1}{\eta_{sa}}\frac{\partial p}{\partial x} \text{ and} \tag{3}$$

$$\frac{1}{r}\frac{\partial}{\partial r}\left(r\frac{\partial u_{sh}}{\partial r}\right) = \frac{1}{\eta_{sh}}\frac{\partial p}{\partial x}. \tag{4}$$

The characteristic Reynolds number for this flow (based on the bulk sheath velocity immediately downstream of the inner capillary exit $U_{sh} = Q_{sh}/\pi R_{sh}^2\left(x = 0^+\right)$ and diameter $2R_{sh}\left(x = 0^+\right)$) is in the range of order 10 to 100. The compatibility, no-slip boundary conditions, and interface conditions are respectively

$$u_{sa}(r = 0) \text{ is finite}, \tag{5}$$

$$u_{sh}(r = R_{sh}) = 0, \tag{6}$$

$$u_{sa}(r = r_{sa}^-) - u_{sh}(r = r_{sa}^+) = 0, \text{ and} \tag{7}$$

$$\eta_{sa}\left.\frac{\partial u_{sa}}{\partial r}\right|_{r=r_{sa}^-} - \eta_{sh}\left.\frac{\partial u_{sh}}{\partial r}\right|_{r=r_{sa}^+} = 0. \tag{8}$$

Here, u_{sa} and $_{sa}$ are respectively the x component of velocity and the dynamic viscosity within the sample stream (u_{sh} and $_{sh}$ correspond to the sheath stream), p is the pressure, and R_{sh} is the radius of the middle, sheath-flow capillary. The "-" and "+" superscripts refer to an r coordinate which approaches r_{sa} from respectively $r < r_{sa}$ and $r > r_{sa}$. The solutions to equations 3 and 4, subject to eqs. 3-6, are given by

$$u_{sa}(r) = \left(\frac{r^2 - r_{sa}^2}{4\eta_{sa}} + \frac{r_{sa}^2 - R_{sh}^2}{4\eta_{sh}}\right)\frac{dp}{dx},\ 0 \le r \le r_{sa} \text{ and} \tag{9}$$

$$u_{sh}(r)=\left(\frac{r^2-R_{sh}^2}{4\eta_{sh}}\right)\frac{dp}{dx},\ r_{sa}<r\le R_{sh}\,. \tag{10}$$

Next, r_{sa} is related to the experimentally controlled parameters of sample and sheath volumetric flow rates, respectively Q_{sa} and Q_{sh}, given by

$$Q_{sa}=\int_0^{r_{sa}}u_{sa}(r)2\pi r dr=\left(\frac{-r_{sa}^4}{\eta_{sa}}+\frac{2\left(r_{sa}^4-r_{sa}^2R_{sh}^2\right)}{\eta_{sh}}\right)\frac{\pi}{8}\frac{dp}{dx}\ \text{and} \tag{11}$$

$$Q_{sh}=\int_{r_{sa}}^{R_{sh}}u_{sh}(r)2\pi r dr=\left(\frac{\left(R_{sh}^2-r_{sa}^2\right)^2}{\eta_{sh}}\right)\frac{\pi}{8}\frac{dp}{dx}\,. \tag{12}$$

Finally, the radius of the sample and sheath streams are shown to vary with the nondimensional flow rate $\bar{Q}=Q_{sh}/Q_{sa}$ and viscosity $\bar{\eta}=\eta_{sh}/\eta_{sa}$ ratios, given by

$$r_{sa}^2=\frac{R_{sh}^2}{1+\bar{Q}\left(1+\sqrt{\bar{\eta}/\bar{Q}}\right)}\,. \tag{13}$$

Equation 13 is a general solution for the variation of an inner (sample) stream tube radius within an outer, co-flowing (sheath) stream where the two streams have different viscosities and flow rates. In the mixer described here, $R_{sh}=R_{sh}(x)$ is modeled as a fifth order polynomial with appropriate first, second, and third type boundary conditions at $x=0$ and $x=L$. The boundary conditions are chosen so that R_{sh} matches the geometry of the experimental device. In experiments where $\bar{Q}$ $\bar{\eta}$ and $\bar{Q}$ 1 (typical in reaction kinetics studies), equation 13 reduces to

$$r_{sa}=R_{sh}\sqrt{\frac{Q_{sa}}{2Q_{sh}}}\,. \tag{14}$$

S5.2 Entrance length effects. Upstream of the fully developed region of the mixer, the sample stream tube begins with an initial radius R_{sa} (the inner radius of the sample capillary). An "entrance length" L_e, associated with the rapid acceleration of the sample stream, is defined as the x position after which the sample stream has been hydrodynamically focused. We hypothesize the sample stream becomes focused after sheath momentum diffuses into the sample stream tube. To this end, we implemented a simple scaling relation for this entrance length of the form $L_e=0.05\mathrm{Re}_{sh}(2R_{sa})$ where Re_{sh} is a Reynolds number based on the diameter of the middle capillary $2R_{sh}$. We determined the 0.05 as a best fit to observed entrance lengths for flow conditions considered here. Further, for simplicity, we propose a heuristic solution for the shape of the area reduction of the sample stream and pose a simple exponential decay (in the axial direction) that approaches the fully developed radius at $x=L_e$. Following these scaling relations, the corrected radius $r_{sa}^{L_e}$ is given by

$$r_{sa}^{L_e} = \begin{cases} R_{sa} \exp\left(\dfrac{x}{L_e} \ln\left(\dfrac{r_{sa}(x = L_e)}{R_{sa}} \right) \right), & 0 \le x < L_e \\ r_{sa}, & L_e \le x \le L \end{cases}. \tag{15}$$

The first region corresponds to the rapid acceleration by the sheath flow as the sample stream first exits the inner capillary (see Figure S8). The factor of R_{sa} before the exponential and the natural log term are respectively the results of the $r_{sa}^{L_e}\left(x=0\right)=R_{sa}$ and the $r_{sa}^{L_e}\left(x=L_e\right)=r_{sa}\left(L_e\right)$ boundary conditions. The second region assumes fully developed flow within the tapered capillary. The latter assumption is similar to that made in lubrication theory [12] for a slowly tapering capillary.

S5.3 Convection-diffusion of species. As described in the current paper, the model considers the radial transport of sample and sheath species within small streamwise sections Δx of the flow as radial diffusion within a cylinder at the local inner radius of the tapered middle capillary R_{sh} (approximated here as $10r_{sa}$). This treatment of the convection-diffusion problem takes advantage of the fact that the velocities near the center of the secondary capillary are relatively uniform. Hence, the velocities of the diffusing species have a very weak dependence of the local radial position. Accordingly, for each small section Δx, the transport of sample and sheath species is described by

$$\frac{\partial c_{sa}^{(n)}}{\partial t} - D_{sa} \frac{1}{r} \frac{\partial}{\partial r}\left(r \frac{\partial c_{sa}^{(n)}}{\partial r} \right) = 0, \text{ and} \tag{16}$$

$$\frac{\partial c_{sh}^{(n)}}{\partial t} - D_{sh} \frac{1}{r} \frac{\partial}{\partial r}\left(r \frac{\partial c_{sh}^{(n)}}{\partial r} \right) = 0, \tag{17}$$

subject to the compatibility and boundary conditions, respectively

$$c_{sa}^{(n)}(r=0) \text{ and } c_{sh}^{(n)}(r=0) \text{ are finite}, \tag{18}$$

$$c_{sa}^{(n)}(r=10r_{sa}^{(n)}) = 0, \tag{19}$$

$$c_{sh}^{(n)}(r=10r_{sa}^{(n)}) = c_{sh,0}, \tag{20}$$

$$c_{sa}^{(0)} = \begin{cases} c_{sa,0}, & 0 \le r \le r_{sa}^{(n)} \\ 0, & r_{sa}^{(n)} < r \le 10r_{sa}^{(n)} \end{cases}, \text{ and} \tag{21}$$

$$c_{sh}^{(0)} = \begin{cases} 0, & 0 \le r \le r_{sa}^{(n)} \\ c_{sh,0}, & r_{sa}^{(n)} < r \le 10r_{sa}^{(n)} \end{cases}, \tag{22}$$

where n denotes a time step, $c_{sa}^{(n)}$ and D_{sa} are respectively the concentration and diffusivity of sample species ($c_{sh}^{(n)}$ and D_{sh} correspond to sheath species) and $r_{sa}^{(n)}$ is the radius of the non-diffuse sample stream. Importantly, t can here be interpreted as the Lagrangian residence time of the sample stream. This t is approximated as the time-integrated steady velocity field along the center ($r=0$) streamline. See References [4,9,10,13] for similar Lagrangian time definitions. We then solve eqs. 14 and 15, subject to eqs. 16-20, by discretizing the time domain into steps t equal to

$\Delta x/U_{sa}(x(t))$ where U_{sa} is the area-averaged velocity of the sample stream. The discretized solution for sample species is given by

$$c_{sa}^{(n)}(r)=c_{sa}^{(n)}(r=10r_{sa}^{(n)})\left\{1-\sum_{j=1}^{\infty}\frac{J_0(ra_j^{(n)})\cdot\exp\left(-D_{sa}\left(a_j^{(n)}\right)^2\Delta t\right)}{a_j^{(n)}\cdot J_1(10r_{sa}^{(n)}a_j^{(n)})\cdot 5r_{sa}^{(n)}}\right\}$$
$$+\sum_{j=1}^{\infty}\frac{J_0\left(r\left(a_j^{(n)}\right)^2\right)\cdot\exp\left(-D_{sa}\left(a_j^{(n)}\right)^2\Delta t\right)}{J_1^2\left(10r_{sa}^{(n)}\left(a_j^{(n)}\right)^2\right)\cdot 50\left(r_{sa}^{(n)}\right)^2}\int_0^{10r_{sa}^{(n)}}J_0(ra_j^{(n)})c_{sa}^{(n-1)}\left(\frac{r_{sa}^{(n-1)}}{r_{sa}^{(n)}}r\right)rdr \quad , \qquad (23)$$

where the $a_j^{(n)}$ are the roots of $J_0\left(10r_{sa}^{(n)}a_j^{(n)}\right)=0$, and J_0 is the Bessel function of the first kind of order zero [14]. (For the solution of the sheath species concentration field, all $c_{sa}^{(n)}$ and D_{sa} are replaced with $c_{sh}^{(n)}$ and D_{sh}.) Note the diffuse sample and sheath streams scalar fields are "compressed" in the radial direction due to the flow acceleration associated with the middle capillary taper. We take this into account heuristically by imposing a nondimensional prefactor which rescales the entire r-coordinate of the previous time step (diffuse) concentration profile in Equation 23 as follows: $c_{sa}^{(n-1)}\left(\frac{r_{sa}^{(n-1)}}{r_{sa}^{(n)}}r\right)$. The numerical integration is implemented in MATLAB (R2019a, Mathworks, USA).

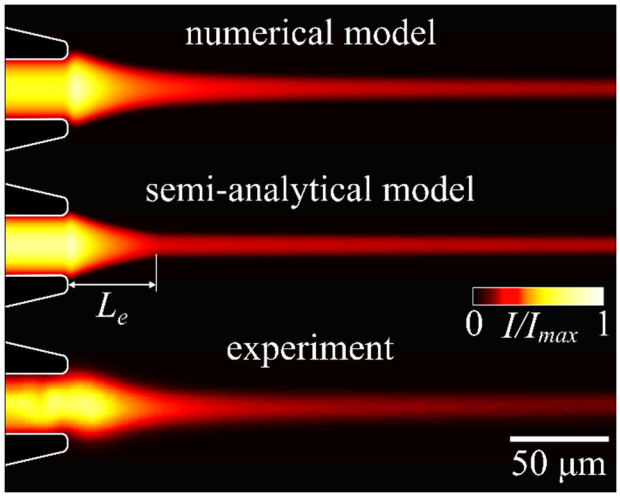

Figure S8. Numerical model (a), semi-analytical model (b), and experimental image (c) of sample concentration field near the inner capillary exit for $Q_{sh}/Q_{sa}=1000$ and $Q_{sh}=0.5\,\mathrm{mL\,min^{-1}}$. The simulated concentration fields were depth-averaged to reproduce the line-of-sight integration of the experimental optics (see section S2). Note the excellent qualitative agreement between simulation and concentration fields. In this operational regime, the transport of the low diffusivity sample species ($D_{sa}=4.25\times10^{-10}$) is dominated by advection and counter-diffusion (away from the center of the sample stream) is negligible.

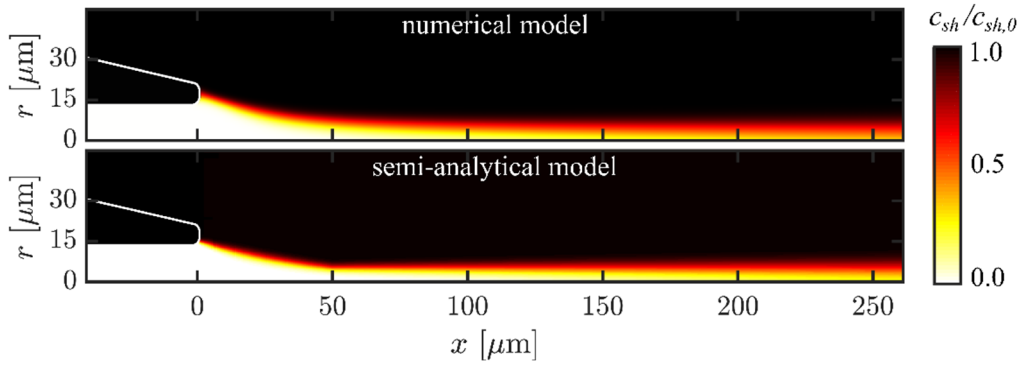

Figure S9. Numerical (a) and semi-analytical (b) sheath concentration fields for the same flow conditions as Figure S8. Note these images have not been depth-integrated and the colorbar has been reversed such that the dark regions of the images (outside of the inner capillary nozzle) correspond to the locations of highest sheath species concentration. In this operational regime, diffusive transport of sheath species is observed (along r) towards the downstream (right-hand-side) of the image.

S6. Parametric exploration of mixing time $t_{0.9}$ for near-complete sheath species diffusion

This section summarizes the variation of the near-complete mixing time, $t_{0.9}$, for varied flow rates and flow rate ratios. The near-complete mixing time is a stricter definition of mixing and is expressed as $t_{0.9} = t\left(\alpha^{-1}(0.9)\right) - t\left(\alpha^{-1}(0.1)\right)$ where α^{-1} denotes the inverse of the mixing degree α (i.e., $\alpha^{-1}(0.1) = x_{0.1}$, the mixing "start" location). This definition is similar to that used by Hertzog et al. [9] for denaturant concentrations diffusing out of a center stream carrying proteins. Figure S10 is analogous to Figure 5d in the current paper, with the left axis (black symbols) being replaced by $t_{0.9}$. This stricter definition of mixing time is useful to quantify the time delay associated with a nearly homogenous concentration of sheath species along the radial direction.

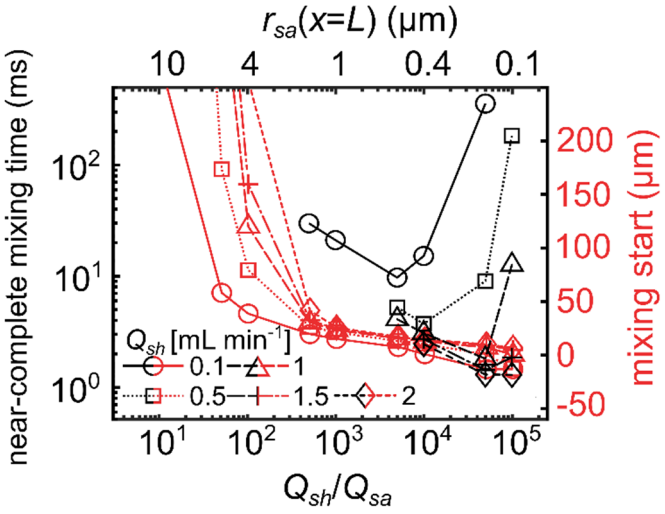

Figure S10. Parametric variation of the near-complete mixing time $t_{0.9}$ (black symbols, left axis) and the streamwise location where mixing commences $x_{0.1}$ (red lines, right axis). The plot is analogous to Figure 5d, although here less flow rate ratio Q_{sh}/Q_{sa} conditions are shown since $Q_{sh}/Q_{sa} < 500$ could not achieve a normalized, area-averaged sheath concentration greater than 0.9. The values of $x_{0.1}$ do not change with this alternative mixing time definition. The lowest value of $t_{0.9}$ achieved here is 1.3 ms for the $Q_{sh}/Q_{sa} = 10^4$, $Q_{sh} = 2\,\text{mL min}^{-1}$. Conversely, the lowest value of t_{mix} achieved is 350 μs for the same flow conditions.

S7. Sample stream tube radii for varied flow rate ratios

Confocal measurements can provide depth-resolved quantification of location of a species throughout a channel cross section. However, accurate confocal imaging is not possible in our mixer as our smallest sample streams have stream tube radii of 0.16 μm and the mixing regions are smaller. The length scales of these flow features are normal to the imaging plane and well beyond the resolution limits of confocal imaging. In table S2 below, we list the radii of the sample stream tube r_{sa} at two locations along the axial direction for the experimental data (for seven values of sheath-to-sample flow rate ratio). These conditions correspond to the experiments described in Figures 3 and 4 of the current paper.

Table S2. Radii of the sample stream tube at two locations downstream of the initial hydrodynamic focusing region.

Q_{sh} / Q_{sa}	$r_{sa}\left(x = 500\mu\text{m}\right)$ (μm)	$r_{sa}\left(x = L = 3\text{mm}\right)$ (μm)
10^2	14	3.5
5×10^2	6.2	1.6
10^3	4.4	1.1
2×10^3	3.1	0.79
5×10^3	2.0	0.50
10^4	1.4	0.35
5×10^4	0.62	0.16

S8. Scaling relation between t_{mix}/t_{stoich} and $c_{sh,0}/c_{sa,0}$

In reaction kinetics experiments, the initial sheath concentration is often relatively high compared to the initial concentration of a precious (and/or expensive) sample species [15,16]. In the current paper, we introduced an "absolute" definition of mixing time, given by

$$t_{mix} = t(\alpha^{-1}(0.5)) - t(\alpha^{-1}(0.1)), \tag{24}$$

where α^{-1} denotes the inverse of the mixing degree α (i.e., $\alpha^{-1}(0.1) = x_{0.1}$, the mixing "start" location). Note t_{mix} is invariant with the initial sample and sheath species concentrations, respectively $c_{sa,0}$ and $c_{sh,0}$.

Alternatively, we also defined a "stoichiometric" mixing time, t_{stoich}, as the time between mixing initiation and the time when an area-averaged sheath species concentration within the sample stream is equal to some proportion of the initial sample concentration. Specifically, for a reaction involving sample A, sheath B, and product AB (given by $n_{sa}A + n_{sh}B \rightarrow n_{AB}AB$ where n_{sa}, n_{sh}, and n_{AB} are stoichiometric coefficients), the stoichiometric mixing time is given by

$$t_{stoich} = t\left(\alpha^{-1}\left(\frac{c_{sa,0}}{c_{sh,0}}\chi\right)\right) - t\left(\alpha^{-1}\left(0.1\frac{c_{sa,0}}{c_{sh,0}}\chi\right)\right), \tag{25}$$

where $\chi = n_{sa}/n_{sh}$ is the ratio of sample to sheath stoichiometric coefficients.

Figure S11 shows predictions of the ratio of stoichiometric mixing time and the "absolute" mixing time versus the ratio of initial species concentrations for varied ratios of stoichiometric coefficients and fixed sheath species diffusivity (all obtained using our semi-analytical model). Shown together with predictions are simple linear regression fits for the data. The comparison suggests t_{mix}/t_{stoich} is linearly proportional to the ratio of initial species concentrations $c_{sh,0}/c_{sa,0}$, i.e.

$$\frac{t_{mix}}{t_{stoich}} = \gamma\frac{c_{sh,0}}{c_{sa,0}}, \tag{26}$$

where γ is the proportionality constant which depends on the sheath species diffusivity and the ratio of stoichiometric coefficients. Values plotted in the figure below are predicted using the diffusivity of iodide ($D_{sh} = 2.5\times10^{-9}$).

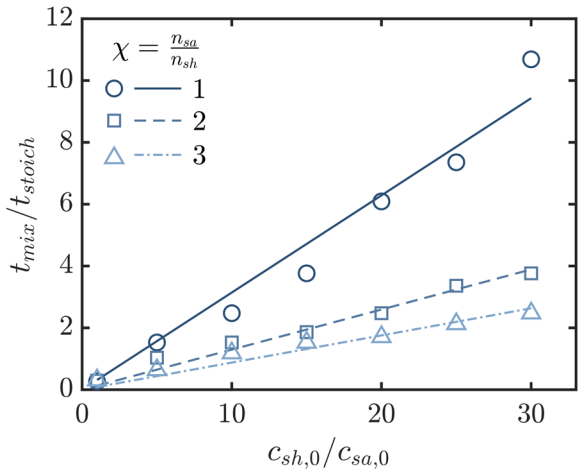

Figure S11. Simulation predictions for the ratio of stoichiometric mixing time to "absolute" mixing time (t_{mix}/t_{stoich}) for varied stoichiometric coefficient ratios $\chi = n_{sa}/n_{sh}$ (as described above) and fixed sheath species diffusivity. Each of these times is associated with the Lagrangian time for sheath species to diffuse into the sample stream. Values plotted in the figure are predicted using a fixed iodide diffusivity ($D_{sh} = 2.5\times10^{-9}$). Importantly, for a fixed value of χ, t_{mix}/t_{stoich} monotonically increases and is approximately directly proportional to $c_{sa,0}/c_{sh,0}$. At $c_{sa,0}/c_{sh,0} = 20$ (i.e. the conditions of our experiments in Section S10), the ratio t_{mix}/t_{stoich} is ~6. The minimum t_{mix} reported in Section 3.3 of the current paper is 350 µs, and the corresponding t_{stoich} is 60 µs.

S9. Sample residence time dependence on flow rate and flow rate ratio

As discussed in the current paper, the sample residence time t is approximated as the residence time of a fluid element which travels from $x = 0$ to some location x' along the center streamline. t is given by

$$t(x) = \int_0^x \frac{dx'}{u(x', r = 0)}, \tag{27}$$

where u is the velocity field.

Figure S12 shows the sample residence time between $x = -2R_{sa}$ (one inner capillary diameter upstream of $x = 0$) and the end of the mixing region $x = L$ versus the flow rate ratio Q_{sh} / Q_{sa} (black symbols, left axis) as well as the sample residence time between the location of mixing start $x = x_{0.1}$ (see Section S6) and $x = L$ (red symbols, right axis).

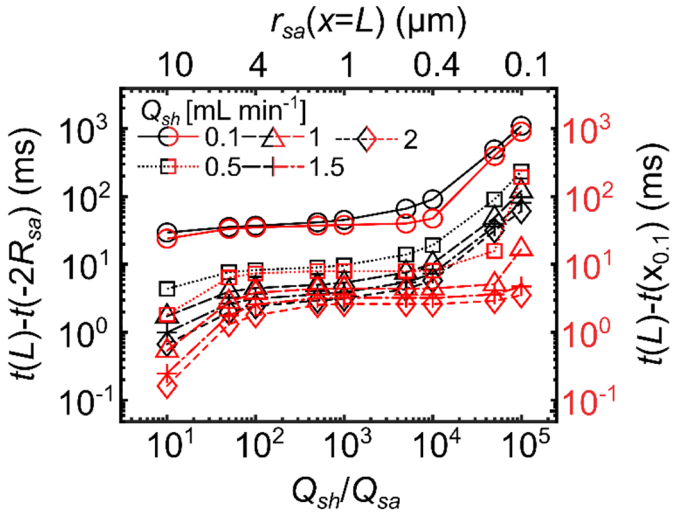

Figure S12. Sample residence time to reach the end of the mixing region $x = L$ versus the flow rate ratio Q_{sh} / Q_{sa} computed from two different start locations, upstream of the inner capillary aperture $x = -2R_{sa}$ (black symbols, left axis) and the location of mixing start $x = x_{0.1}$ (red symbols, right axis). Shown are results for sheath flow rates Q_{sh} between 0.1 and 2 mL min^{-1}. The shortest residence times occur for low values of Q_{sh} / Q_{sa} (less than 50) since the sample momentum contributes significantly to the velocity field. For fixed Q_{sh}, the sample residence time is nearly invariant with Q_{sh} / Q_{sa} values between 10^2 and 10^4. The highest Q_{sh} / Q_{sa} values (greater than 5×10^4) result in significantly longer sample residence times.

S10. Mixer version using polyimide tube in place of outer (expansion) capillary

Compared to borosilicate glass, polyimide films of 100 µm thickness have been shown to provide about twice as much X-ray transmission in the 6-10 keV range [17,18]. Therefore, a polyimide capillary (250 µm inner radius and 350 µm outer radius, MicroLumen, USA) replaced the outer glass capillary of the mixer version used to conduct hard X-ray spectroscopy experiments at the Stanford Synchrotron Radiation Lightsource (SSRL).

Figure S13 shows images of the polyimide outer capillary version of the mixer, recorded over three beamtimes at SSRL (a total of 15 days and ~150 hours of mixer operation). The experiment followed the millisecond timescale binding of cyanide (CN) (100 mM) to met-myoglobin (5 mM) by recording the iron spin-sensitive spectra of Kβ emissions. The use of X-rays in the 6-10 keV range imposed additional constrains to the mixer design and operation. First, a polyimide outer capillary was chosen as it has a high X-ray transmittance and is insensitive to X-ray damage. Second, while X-ray spectroscopy is ideal to study subtle changes in the electronic structures of reacting species, the increased sensitivity comes at the cost of reduced signal-to-noise ratio (SNR). Hence, a low flow rate ratio Q_{sh}/Q_{sa} was chosen to provide a large sample stream within the downstream probing region. We expect to present this study in a future publication.

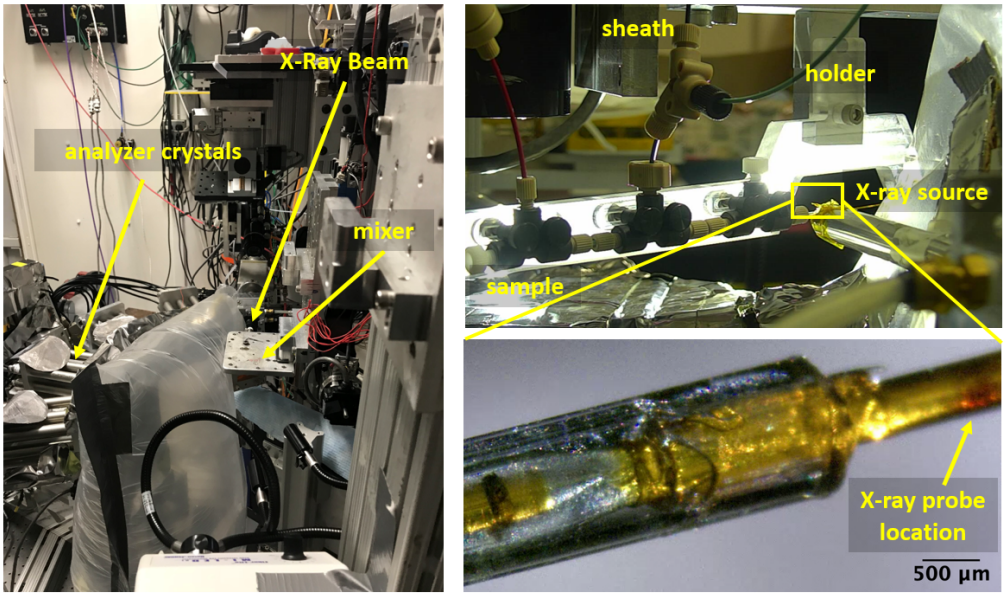

Figure S13. Outer polyimide capillary mixer version. Images recorded during ~150 hours of operation over three separate beamtimes (a total of 15 days) of hard X-ray spectroscopy experiments at the Stanford Synchrotron Radiation Lightsource (SSRL). Ten versions of this mixer (with replaced outer sleeve and varied inner capillary diameter) were used throughout these experiments. In the experimental setups shown here, $Q_{sh}/Q_{sa} = 25$ and $Q_{sh} = 1\,\mathrm{mL\,min^{-1}}$, producing a minimal sample stream diameter (in the middle capillary) of 14 µm and maximum sample stream diameter (in the outer capillary) of 120 µm, which agreed well with the vertical full width at half max of the incoming beam. Polyimide outer capillaries were chosen for these experiments because they have a high X-ray transmittance and are insensitive to X-ray damage.

S11. References

[1] S.A. Pabit, S.J. Hagen, Laminar-Flow Fluid Mixer for Fast Fluorescence Kinetics Studies, Biophys. J. 83 (2002) 2872–2878.

[2] K.M. Hamadani, S. Weiss, Nonequilibrium Single Molecule Protein Folding in a Coaxial Mixer, Biophys. J. 95 (2008) 352–365.

[3] K.S. Burke, D. Parul, M.J. Reddish, R.B. Dyer, A simple three-dimensional-focusing, continuous-flow mixer for the study of fast protein dynamics, Lab. Chip. 13 (2013) 2912.

[4] G.D. Calvey, A.M. Katz, C.B. Schaffer, L. Pollack, Mixing injector enables time-resolved crystallography with high hit rate at X-ray free electron lasers, Struct. Dyn. 3 (2016) 054301.

[5] S. Inoue, K. Spring, Video Microscopy: The Fundamentals, 2nd ed., Springer US, 1997.

[6] J.R. Lakowicz, Principles of Fluorescence Spectroscopy; 3rd edition; Springer, New York, 2006.

[7] W. Voss, R.M. Watt, Solvent Specific Perturbation Antibody of the Fluorescence of Fluorescein Bound to, J. Biol. Chem. 254 (1979) 1684–1690.

[8] J.B. Knight, A. Vishwanath, J.P. Brody, R.H. Austin, Hydrodynamic Focusing on a Silicon Chip: Mixing Nanoliters in Microseconds, Phys. Rev. Lett. 80 (1998) 3863–3866.

[9] D.E. Hertzog, X. Michalet, M. Jäger, X. Kong, J.G. Santiago, S. Weiss, O. Bakajin, Femtomole Mixer for Microsecond Kinetic Studies of Protein Folding, Anal. Chem. 76 (2004) 7169–7178.

[10] D.E. Hertzog, B. Ivorra, B. Mohammadi, O. Bakajin, J.G. Santiago, Optimization of a Microfluidic Mixer for Studying Protein Folding Kinetics, Anal. Chem. 78 (2006) 4299–4306.

[11] P.M. Wheat, J.D. Posner, Quantifying mixing using equilibrium reactions, Phys. Fluids. 21 (2009) 037101.

[12] F.M. White, Viscous Fluid Flow, 3rd ed., McGraw-Hill, Singapore, 2006.

[13] D. Oberthuer, J. Knoška, M.O. Wiedorn, K.R. Beyerlein, D.A. Bushnell, E.G. Kovaleva, M. Heymann, L. Gumprecht, R.A. Kirian, A. Barty, V. Mariani, A. Tolstikova, L. Adriano, S. Awel, M. Barthelmess, K. Dörner, P.L. Xavier, O. Yefanov, D.R. James, G. Nelson, D. Wang, G. Calvey, Y. Chen, A. Schmidt, M. Szczepek, S. Frielingsdorf, O. Lenz, E. Snell, P.J. Robinson, B. Šarler, G. Belšak, M. Maček, F. Wilde, A. Aquila, S. Boutet, M. Liang, M.S. Hunter, P. Scheerer, J.D. Lipscomb, U. Weierstall, R.D. Kornberg, J.C.H. Spence, L. Pollack, H.N. Chapman, S. Bajt, Double-flow focused liquid injector for efficient serial femtosecond crystallography, Sci. Rep. 7 (2017) 46846.

[14] J. Crank, The Mathematics of Diffusion, Oxford University Press, 1975.

[15] Yi-Ling Hsieh, Tsung-Yi Ho, K. Chakrabarty, A Reagent-Saving Mixing Algorithm for Preparing Multiple-Target Biochemical Samples Using Digital Microfluidics, IEEE Trans. Comput. Des. Integr. Circuits Syst. 31 (2012) 1656–1669.

[16] J.-D. Huang, C.-H. Liu, T.-W. Chiang, Reactant minimization during sample preparation on digital microfluidic biochips using skewed mixing trees, in: Proc. Int. Conf. Comput. Des. - ICCAD '12, ACM Press, New York, New York, USA, 2012: p. 377.

[17] B.L. Henke, E.M. Gullikson, J.C. Davis, X-Ray Interactions: Photoabsorption, Scattering, Transmission, and Reflection at E = 50-30,000 eV, Z = 1-92, At. Data Nucl. Data Tables. 54 (1993) 181–342.

[18] E. Gullikson, Filter Transmission, (2010).